Pergamon

Int. J. Solids Structures Vol. 35, No. 19, pp. 2537–2566, 1998
© 1998 Elsevier Science Ltd
All rights reserved. Printed in Great Britain
0020–7683/98 $19.00 + .00

PII: S0020–7683(97)00143–1

FRACTURE OF RANDOM MATRIX–INCLUSION COMPOSITES: SCALE EFFECTS AND STATISTICS

K. ALZEBDEH
Electromotive Division, General Motors Corp., 55th Street, La Grange, IL 60525-8051, U.S.A.

A. AL-OSTAZ
Department of Materials Science and Mechanics, Michigan State University, East Lansing, MI 48824-1226, U.S.A.

I. JASIUK
George W. Woodruff School of Mechanical Engineering, Georgia Institute of Technology, Atlanta, GA 30332-0405, U.S.A.

M. OSTOJA-STARZEWSKI
Institute of Paper Science and Technology, and Georgia Institute of Technology, 500 10th Street, N.W., Atlanta, GA 30318-5794, U.S.A.
E-mail: martin.ostoja@ipst.edu

(*Received* 19 *May* 1997)

Abstract—We study crack patterns and effective stress–strain curves in unidirectional fiber–matrix composites subjected to a uniform out-of-plane shear. The fibers are aligned in the longitudinal direction and arranged randomly, with no overlap, in the transverse plane. Both fibers and matrix are isotropic and elastic–brittle. We conduct this analysis numerically using a very fine two-dimensional spring network and simulate the crack initiation and propagation by sequentially removing bonds which exceed a local fracture criterion. In particular, we focus on effects of scale and geometric randomness in these composites. We consider several "windows of observation" (scales) and study crack patterns, types of constitutive responses, and statistics of the corresponding scale dependent effective elastic stiffness and strength of such composites. In the parametric study we cover a wide range of material combinations defined by the stiffness ratio and the strain-to-failure ratio and we employ a damage plane in terms of these two parameters to illustrate the results. © 1998 Elsevier Science Ltd. All rights reserved.

1. INTRODUCTION

Statistical uncertainty in strength properties of engineering materials has been a known problem for decades. Some of the earliest studies on the subject date back to the twenties and thirties, when Weibull (1939) introduced his well known probability fits. However, due to the complexity of the problems and lack of adequate tools, these derivations had to be based on rather simplistic treatments of mechanics of microstructures with defects; they relied, basically, on very insightful probabilistic arguments. This situation of statistical strength theories continued for many decades, while on a parallel, and quite independent track the fracture mechanics made great strides. Fracture mechanics has essentially been developing as a deterministic science perfectly suited for treatment of a single crack in a homogeneous material, rather than for analysis of fields of many cracks and failure evolution in heterogeneous microstructures. The lack of adequate tools for treatment of such problems was sorely felt in damage mechanics, which is characterized by an interplay of many cracks in disordered materials. The situation has changed over a recent decade due to the advent of computational mechanics and powerful computers, which now begin to permit a "brute force" simulation of complex fracture events; these are the tools that were not available to Weibull and his contemporaries.

As far as the computational fracture mechanics is concerned, two principal methods are available: finite elements and spring networks. The second one is borrowed from the condensed matter physics; it relies on a regular lattice representation of a homogeneous

continuum, which avoids any mesh generation (preprocessing) that is a problem with finite elements. This means that heterogeneous media can easily be modeled by assigning the spring constants all over the lattice according to the local phase properties. The second major advantage of spring networks is the possibility to create cracks by removing the spring bonds without any need for remeshing that is often required in simulations of crack propagation by finite elements. For slow phenomena one simulates the crack evolution in a quasi-static manner, while for dynamic problems one introduces the inertia forces to turn the method into a variant of molecular dynamics.

Various studies related to the present one have recently been conducted using similar tools in the fracture/damage mechanics of composite materials. Several symposia, conferences, journal special issues, and books reflect the activity in this area [e.g. Charmet *et al.* (1990); Herrmann and Roux (1990; Huet (1993); Bazant *et al.* (1994); Breysse (1994); Pyrz (1995); Carpinteri (1996); Krajcinovic (1996); Pineau and Zaoui (1996); van Mier (1996); Ostoja-Starzewski (1997)].

The present paper exploits this spring network method for the analysis of fracture characteristics of a two-dimensional matrix–inclusion composite with locally isotropic elastic–brittle phases. We continue the research program begun in (Ostoja-Starzewski *et al.* 1994a, b) with the main objective of developing a framework of stochastic fracture and damage mechanics for a class of random composites in which fibers are randomly distributed in the matrix. More specifically, crack initiation and propagation as well as effective responses in two-dimensional brittle matrix-fiber composites are studied for the anti-plane elasticity problem under a uniform shear loading. This problem is equivalent, by virtue of analogies, to elastic membrane, thermal conductivity, electrical conductivity, etc., since they are all governed locally by a Laplace's equation. A related problem of in-plane response has been studied in (Ostoja-Starzewski and Lee, 1996).

We study damage patterns and effective stress–strain responses as a function of several parameters: mismatch of elastic properties of matrix and inclusions, mismatch of strength properties of matrix and inclusions, and scale of a test window with which simulations are being conducted. We display the results in a so-called damage plane, that is a plane of both mismatch parameters, and we call such results damage maps. Three scales of test windows are being investigated; they constitute meso-scale statistical continuum approximations of a random composite. For each of these scales we establish the best probability fits of random stiffnesses and random strengths.

2. RANDOM COMPOSITE AND ITS SPRING NETWORK REPRESENTATION

2.1. *Model of a random composite*

Of concern in this paper is the anti-plane response of a unidirectional fiber composite material in the plane transverse to the axis of the fiber alignment. A typical cross-section of such a composite is shown in Fig. 1(a), where two aspects are immediately noted: spatial

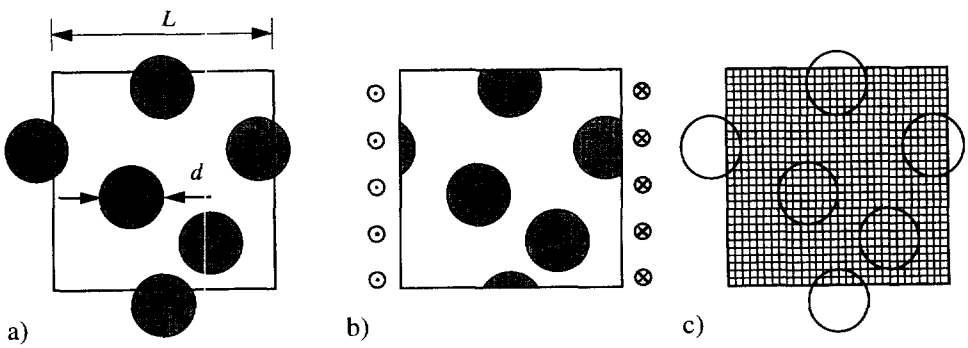

Fig. 1. (a) A disordered matrix–inclusion composite with inclusions of average diameter d and periodicity L, showing a periodic window of scale $\delta = L/d$; (b) a schematic of loading of the periodic window via periodic boundary conditions (2); (c) a fine mesh spring network with local springs is shown.

disorder and periodicity on the scale of the window L. The spatial disorder is a feature of primary interest in this study, and thus, a formalism of random media theory has to be adopted [e.g. Beran (1968)], in that the specimen of Fig. 1(a) is one deterministic realization $\mathbf{B}(\omega)$ of the random matrix–inclusion composite. The latter is taken as a set $\boldsymbol{B} = \{\mathbf{B}(\omega);\ \omega \in \Omega\}$, where ω is an element of the underlying sample (probability) space Ω. The ω's are realizations of a planar Poisson point process; each ω specifies the centers of all the circular inclusions in a given window. This Poisson process is subject to a condition of inhibition in the sense that a new point is accepted providing it does not fall closer than a certain minimum distance with respect to any of the previous ones; this is also called a random sequential addition (Torquato, 1988). In order to avoid the problem of arbitrarily narrow necks between inclusions, we take the distance between the centers of inclusions to be somewhat greater than the inclusions' diameter d; we return to this issue in Section 2.2.

Our interest is in the effective response of the random medium on scales finite with respect to the inclusion size. The effective response in such a situation will strongly depend on the type of boundary conditions. For example, one could consider kinematic (displacement-controlled) boundary conditions which would lead to a stable crack propagation, or force (stress-controlled) boundary conditions, which would result in an unstable fracture. The drawback of these two types of conditions lies in the need for an arbitrary interpretation or modification of the microstructure: (i) either isolate a test window "at random" from a theoretically infinite disordered composite, which would result in some inclusions being cut at the window boundaries; or (ii) modify the microstructure in the boundary zone so as to avoid any such non-physical cutting of the inclusions.

To obviate this issue of boundary effects, we introduce a periodicity on the scale L, as shown in Fig. 1(a). This immediately defines a dimensionless parameter

$$\delta = \frac{L}{d} \tag{1}$$

which specifies the length scales of material disorder, and thus, the size of a mesoscale element, which may be called a statistical volume element (SVE) [see also Jeulin *et al.* (1997)]. Let us note that now, the SVE is the random medium $\boldsymbol{B}_\delta = \{\mathbf{B}_\delta(\omega);\ \omega \in \Omega\}$. Appropriate for such a periodic SVE is a strain-controlled periodic boundary condition, which for the anti-plane response under consideration is written as

$$\begin{aligned} u(\mathbf{x}+\mathbf{L}) &= u(\mathbf{x}) + \boldsymbol{\varepsilon}^0 \cdot \mathbf{x} \\ \mathbf{t}(\mathbf{x}+\mathbf{L}) &= -\mathbf{t}(\mathbf{x}) \quad \forall \mathbf{x} \in \partial \mathbf{B}_\delta \end{aligned} \tag{2}$$

where $u = u_3$ (out-of-plane displacement), $\boldsymbol{\varepsilon}^0 = (\varepsilon^0_{13}, \varepsilon^0_{23})$ is a given constant strain, and $\mathbf{t} = (\sigma_{13} n_1, \sigma_{23} n_2)$ is the surface traction. Also, $\mathbf{L} = L\mathbf{e}$ with $\mathbf{e}$ being a unit vector, and $\partial \mathbf{B}_\delta$ is the boundary of $\mathbf{B}_\delta$. Figure 1(b) shows the situation for $\boldsymbol{\varepsilon}^0 = (\varepsilon^0_{13}, 0)$, which will henceforth be the loading case of choice in this paper; thanks to the isotropy of the Poisson point process of disks' placement no generality is lost. It is important to note that due to the introduction of periodicity on the length scale L, a relatively weak variability will be observed for small δ compared to what would be obtained under other type of boundary conditions (kinematic, force, and mixed); we study this entire issue in (Alzebdeh *et al.*, 1998).

Both phases of the composite material are taken to be linear elastic, locally isotropic and homogeneous; they are described by $C^{\mathrm{i}}_{ij} = C^{\mathrm{i}} \delta_{ij}$ and $C^{\mathrm{m}}_{ij} = C^{\mathrm{m}} \delta_{ij}$ for the inclusions (i) and the matrix (m), respectively. Thus, the governing equation of this piecewise-constant material is

$$C\left(\frac{\partial^2 u}{\partial x_1} + \frac{\partial^2 u}{\partial x_2}\right) = 0 \quad C = C^{\mathrm{i}}, C^{\mathrm{m}} \quad u \equiv u_3. \tag{3}$$

The boundary condition eqn (2) on any sample composite $\mathbf{B}_\delta(\omega)$ results in an effective random stiffness tensor $\mathbf{C}_\delta(\omega)$, with the constitutive law being stated as

$$\bar{\boldsymbol{\sigma}}(\omega) = \mathbf{C}_\delta(\omega) \cdot \boldsymbol{\varepsilon}^0. \tag{4}$$

The ω-dependence in eqn (4) points to a random nature of the resulting stress field and of the effective stiffness tensor (overbar indicates a volume average), with the fluctuations disappearing in the limit $\delta \to \infty$. Moreover, eqn (4) is the basis for introducing an effective, equivalent continuum on the given scale δ, and hence the $\mathbf{C}_\delta(\omega)$ notation. In this paper we study three scales $\delta = 2.2, 4.5$ and 9.1 numerically, and determine the corresponding damage patterns, effective constitutive laws, and the statistics of effective stiffness and strength.

2.2. *Spring network discretization*

The continuum composite (the transverse plane of a fiber–matrix composite) is discretized using a square spring network [Fig. 1(c)]; we follow here the approach discussed in our earlier papers (Ostoja-Starzewski *et al.*, 1994a, 1996, 1997). Thus, the stiffness tensor of a unit cell of this spring network, modeling an isotropic continuum, is given as

$$C_{11} = C_{22} = \frac{k}{2} \quad C_{12} = C_{21} = 0 \tag{4}$$

where k is half the bond spring constant. The spring network discretization of the composite is based on the fact that the inclusion diameters d are several times larger than the lattice spacing. In fact, we had earlier chosen d to be 14 times the lattice spacing so as to approximate to within two percent the mean field response of a dilute composite which is known exactly (Sheng, 1995).

As can be gleaned from Fig. 1(c), the coordinates of Poisson points are rounded off so as to place the disk centers on the nodes of the spring network. The resolution of stress and other dependent fields in the narrow necks between the inclusions can only be approximate and so we force the disks' centers to be at least two lattice spacings apart. Next, the spring constants of matrix and inclusion bonds (k^{m} and k^{i}) are assigned according as they fall in a given phase, while any bond straddling the circular matrix–inclusion boundaries has its spring constant k^{b} assigned according to a series spring system weighted by the partial lengths (l^{m} and l^{i}) of the bond that belong to the respective domains, that is

$$k^{\mathrm{b}} = \left(\frac{l^{\mathrm{m}}}{lk^{\mathrm{m}}} + \frac{l^{\mathrm{i}}}{lk^{\mathrm{i}}} \right)^{-1} \qquad l = |l^{\mathrm{b}}| = l^{\mathrm{m}} + l^{\mathrm{i}}. \tag{5}$$

The key unknown in the spring network problem is the displacement field $u(i,j)$ over the window domain. This is, essentially, a linear algebra problem of as many degrees-of-freedom as there are nodes in the network. A solution is accomplished by employing a conjugate gradient method [e.g. Press *et al.* (1992)] with respect to the total energy (sum of energies stored in all the spring bonds) and subject to the boundary condition eqn (2). With the $u(i,j)$ solution at hand, the total potential energy E stored in the network provides a basis for determination of the equivalent, effective medium mentioned in connection with eqn (3), according to the relation

$$E = \frac{V_\delta}{2} \boldsymbol{\varepsilon}^0 \cdot \mathbf{C}_\delta(\omega) \cdot \boldsymbol{\varepsilon}^0. \tag{6}$$

In eqn (6) V_δ is the volume of $\mathbf{B}_\delta(\omega)$.

2.3. *Fracture simulations*

One of the principal advantages of spring networks lies in a possibility of simulating fracture events, such as simultaneous growth of many cracks, through the removal of spring bonds in accordance with their exceeding local failure criteria, while taking full account of the resulting stress redistribution throughout the lattice. Given a two-phase composite, two

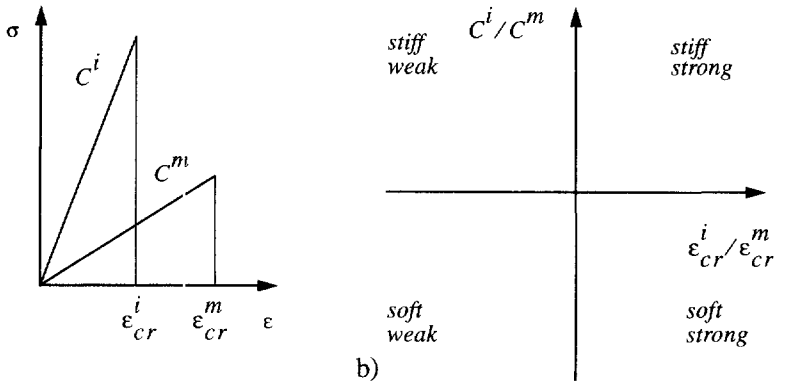

Fig. 2. (a) Elastic–brittle stress–strain curves for matrix and inclusion materials; (b) sketch of the damage plane.

failure criteria are needed in our problem: failure of matrix bonds and failure of inclusion bonds. We choose to express them in terms of a bond strain

$$\varepsilon^{\mathrm{m}} \geqslant \varepsilon^{\mathrm{m}}_{\mathrm{cr}} \quad \text{and} \quad \varepsilon^{\mathrm{i}} \geqslant \varepsilon^{\mathrm{i}}_{\mathrm{cr}}, \tag{7}$$

but it is important to point out that, for an elastic–brittle material, this is fully equivalent to (i) a criterion in terms of stress (or force) carried by a given bond, or (ii) a criterion in terms of the energy stored in a given bond.

The failure criterion of any bond straddling the circular matrix–inclusion boundaries is assigned as follows: it is weighted by the partial lengths (l^{m} and l^{i}) of the bond that belong to the respective domains, that is

$$\varepsilon^{\mathrm{b}} = \frac{l\varepsilon^{\mathrm{m}}}{l^{\mathrm{m}}} + \frac{l\varepsilon^{\mathrm{i}}}{l^{\mathrm{i}}} \quad l = |\mathbf{l}^{\mathrm{b}}| = l^{\mathrm{m}} + l^{\mathrm{i}}. \tag{8}$$

Now, one of the basic questions is this: given a composite made of two different elastic–brittle phases, is its effective response also elastic–brittle or not? The spring network method provides a convenient way to answer this question for a wide range of parameters. At this stage we note that two other types of responses are also possible: post-peak and pre-peak depending on whether damage occurs after or prior to the peak $\sigma_{\max}$ in the effective stress–strain curve (Fig. 3).

There are two ways to simulate fracture. The first one proceeds in the following steps:

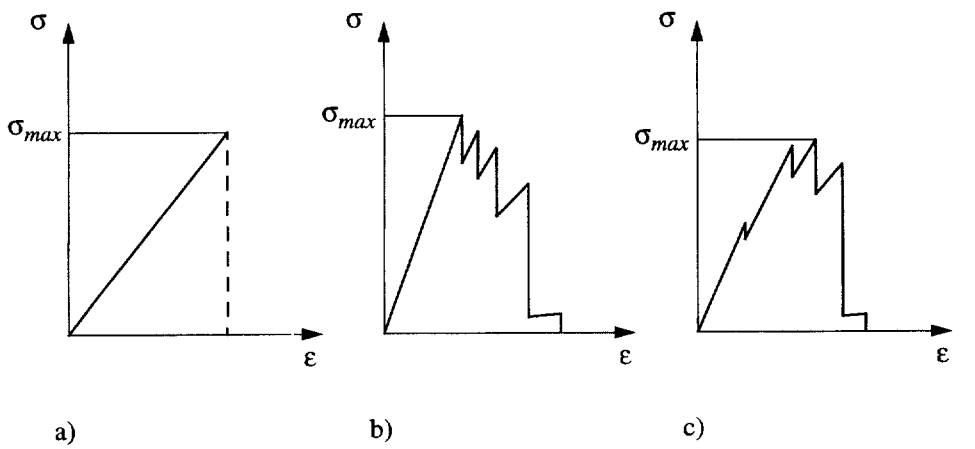

Fig. 3. Effective stress–strain curves: (a) elastic–brittle; (b) post-peak; and (c) pre-peak.

(1) We load the spring network by subjecting it to a small initial strain ε^0 under the periodic boundary condition eqn (2), and solve for the equilibrium state by a conjugate gradient method.

(2) We next search, under ε^0, for any spring in the lattice whose strain exceeds the local fracture criteria eqn (7). If eqn (7) is not met anywhere, we increment the initial strain ε^0, solve for the equilibrium, and check eqn (7) again. The process is being repeated until eqn (7) is met.

(3) Once eqn (7) is met at some strain ε^n (by the nth increment), the spring is removed from the network, thus representing an increment of a crack propagation process. The system must now be re-equilibrated at the given strain ε^n, and condition eqn (7) must be applied again to all the surviving bonds. Should any one of those bonds be failing this check, it needs to be removed, and the network needs to be re-equilibrated again. This process is continued until no more springs are failing at the given load ε^n. A range of scenarios is possible here: either just one bond needs to be removed at a given load level, or a number of them fail, but the system retains some load-carrying capability and can be strained further, or the bonds need to be removed from the lattice until a crack cuts it entirely. The latter is a situation of global brittle response.

(4) The process of incrementing the strain of condition eqn (2) and checking for local failures as described in point (3) is being continued until a continuous crack path is formed through the whole specimen.

The second way to simulate fracture proceeds in these steps:

(1) Same as step 1 above.

(2) Since the system is linear elastic, we can infer from the current strain levels of all the bonds which one of them is most likely to fail (i.e. reach ε_{cr}^m or ε_{cr}^i) under an increasing global strain. We can, therefore, infer this strain directly, and remove this "hottest" bond immediately without making many small steps.

(3) Same as step (3) above.

(4) Repeat steps (2) and (3) until a continuous crack path is formed through the whole specimen.

Clearly, the advantage of this second method is the possibility to avoid applying a number of strain increments outlined in point (2) of the first method, and this is a chosen procedure in our study.

Such a spring network approach to modeling fracture evolution was recently tested in a much more complex, in-plane, rather than anti-plane, loading situation (Grah *et al.*, 1996). This involved fracture of a very thin polycrystalline aluminum sheet made of some 40 crystals, where over 90% agreement of observed and simulated crack patterns was attained. The advantages of spring network models as opposed to other numerical techniques (such as finite elements) hinge on their efficiency to simulate crack formation in highly complicated systems with a very large number of degrees of freedom. It is noteworthy that no remeshing of the domain is needed (as in finite elements) nor is it limited to cases of pre-known basic exact solutions (as in boundary elements).

3. CRACK PATTERNS AND EFFECTIVE STRESS–STRAIN CURVES

3.1. *Interpretation in terms of strain strengths*

All numerical simulations reported in this paper are carried out under a uniform out-of-plane strain $\varepsilon^0 = (\varepsilon_{13}^0, 0)$, using three different window sizes: $L = 31, 63, 127$ lattice units, and the diameter of inclusions $d = 14$ units, giving us three scales $\delta = L/d = 31/14 \cong 2.2$, $\delta = 63/14 = 4.5$, $\delta = 127/14 \cong 9.1$, at the same volume (area) fraction of inclusions $f = 35\%$. Note that the intermediate scale ($\delta = 4.5$) has been studied in Jasiuk *et al.* (1994) and Ostoja-Starzewski *et al.* (1994a, 1997). The above three δ sizes, in particular $\delta = 2.2$ and 4.5 define a rather small scale of composite, but they allow a comparatively rapid simulation of damage.

As discussed in Section 2 both matrix and inclusions are linear-elastic and brittle, and their constitutive responses are defined by the stiffnesses C^m, C^i and strains-to-failure $\varepsilon_{cr}^m, \varepsilon_{cr}^i$ [see Fig. 2(a)]. Thus, in this section we explore the effects of two parameters, the *stiffness ratio* C^i/C^m and the *strain-to-failure ratio* $\varepsilon_{cr}^i/\varepsilon_{cr}^m$, and study their influence on damage patterns and effective stress–strain curves for each of the three scales (window sizes) $\delta = 2.2$, 4.5, 9.1. For this purpose, following Ostoja-Starzewski *et al.* (1997), we employ the *damage plane* such that the horizontal axis represents $\varepsilon_{cr}^i/\varepsilon_{cr}^m$, while the vertical axis denotes C^i/C^m; a representation of a given property in this plane we call a *damage map*. We vary C^i/C^m and $\varepsilon_{cr}^i/\varepsilon_{cr}^m$ as 0.1, 1 and 10, which gives us nine cases. A schematic of such a plane is shown in Fig. 2(b) and it is used in Figs 4–12. The top row corresponds to the case of inclusions ten times stiffer than the matrix, the middle one to the composite with fibers having the same stiffness as the matrix and the bottom row when inclusions are 10 times more compliant (softer) than the matrix. Thus, as we move up the plane the stiffness of inclusions increases. Similarly, as we move from left to right the strain strength of inclusions increases. The left column denotes the cases when inclusions are 10 times weaker in strain strength than the matrix, $\varepsilon_{cr}^i/\varepsilon_{cr}^m = 0.1$ (we refer to this case as weak inclusions case in terms of strains), the middle column represents the cases when inclusions have the same strain strength as the matrix, and the right one when inclusions have higher strain strength than the matrix, $\varepsilon_{cr}^i/\varepsilon_{cr}^m = 10$ (we refer to this case as a strong inclusion case in terms of strains). Thus, the center of the damage plane represents a perfectly homogeneous case in which the stiffnesses and strengths of both inclusions and the matrix are identical, while the left bottom corner represents the case of soft and weak (in terms of strain) inclusions, the right bottom corner the case of soft and strong inclusions, the left top corner stiff and weak inclusions and the right top corner stiff and strong inclusions.

The results for three window sizes are shown in Figs 4–12; results for the scale $\delta = 2.2$ are given in Figs 4–6, for $\delta = 4.5$ in Figs 7–9, and for $\delta = 9.1$ in Figs 10–12. Figures 4, 7 and 10 give the stress contours fields obtained using ABAQUS, Figs 5, 8 and 11 show crack patterns obtained by spring networks, and Figs 6, 9 and 12 give effective stress–strain curves obtained using spring networks.

In Fig. 5 we show a damage map of crack/damage patterns at scale $\delta = 2.2$ for a single realization. For each parameter combination we give two crack patterns: the top one representing the state of a partial damage and the one underneath giving the state of final crack patterns in a window. The former one, chosen rather arbitrarily, illustrates an early stage of damage and, thus, gives the information on where cracks initiated. Figure 4 shows strain contours $\varepsilon_{13}/\varepsilon_{cr}$ in the virgin system of matrix and inclusions, obtained by a finite element program ABAQUS for the same realization. These strain contours are divided by strain strengths to illustrate the locations of maximum relative strains and thus possible conditions for crack initiation.

Starting with the bottom row where $C^i/C^m = 0.1$ and the left corner ($\varepsilon_{cr}^i/\varepsilon_{cr}^m = 0.1$) we have the case of soft and weak inclusions. Thus, it is not surprising that in this case the cracks initiate in the inclusions (in locations closest to a neighboring inclusion) and there is a considerable damage in the inclusions before the crack cuts across the matrix. The strain contours also clearly point to inclusions as "hot spots". A similar response is observed for the middle case of inclusions ten times softer than the matrix but having identical strains-to-failure. In fact the locations of crack initiation are the same, but overall there is less cracking in the inclusions prior to failure. This smaller amount of damage in the inclusions is due to the fact that now the matrix experiences higher relative strains and thus fractures earlier. This is also clearly seen from the strain contour of Fig. 4 for this case. The right corner of the bottom row in the damage plane is the case of soft and strong inclusions (in terms of strain), $C^i/C^m = 0.1$ and $\varepsilon_{cr}^i/\varepsilon_{cr}^m = 10$, and the cracks initiate in the matrix for this parameter combination. A glance at the contours of relative strains confirms the fact that the crack initiation will occur in the matrix.

The middle row in the damage plane represents the case when stiffnesses of inclusions and the matrix are equal ($C^i/C^m = 1$); this gives uniform stress fields everywhere in the material. In addition, when the strain stengths are equal ($\varepsilon_{cr}^i/\varepsilon_{cr}^m = 1$) we have the case of a homogeneous material with same stiffnesses and strengths throughout. This is a trivial case

which gives a uniform damage throughout and thus the crack patterns are omitted. When both constituents have the same stiffness, but $\varepsilon^i_{cr}/\varepsilon^m_{cr} = 0.1$, i.e. inclusions are weaker than the matrix, the inclusions crack first, as expected, before the crack propagates across the matrix. In this case all bonds in the inclusions break simultaneously since the stress field is uniform. The contours of relative strains show uniform fields with inclusions being "hot spots" due to their lower strength. When $\varepsilon^i_{cr}/\varepsilon^m_{cr} = 10$, i.e. inclusions are stronger than the matrix in terms of strains, and the stiffnesses are the same, the damage occurs only in the matrix. In this situation all bonds break simultaneously in the matrix, again, due to a uniform state of stress. This is also clearly seen from the strain contours which show uniform fields with matrix having lower relative strain strength.

When $C^i/C^m = 10$ (top row) and $\varepsilon^i_{cr}/\varepsilon^m_{cr} = 0.1$ (left corner), i.e. inclusions are stiff and weak in strain, the cracks initiate in the inclusions. Note that again cracks initiate in the "hot spots" shown by strain contours of Fig. 4. In the case of inclusions 10 times stiffer than the matrix and $\varepsilon^i_{cr}/\varepsilon^m_{cr} \geqslant 1$ cracks initiate and propagate only in the matrix. It is interesting to note that the cases $\varepsilon^i_{cr}/\varepsilon^m_{cr} = 1$ and 10 give identical crack patterns. This is due to the fact that damage is matrix dominated.

From both the crack patterns of Fig. 5 and strain contours of Fig. 4 we can additionally observe that when inclusions are strong in strains the maximum relative strains occur in the matrix, and when the inclusions are soft the cracks initiate at locations perpendicular to the x_1-(horizontal) direction, while for the case of stiff inclusions along a line parallel to x_1-axis, when ε^0_{13} is applied. This response is analogous to the in-plane elasticity case when a composite is subjected to a uniaxial tension in the x_1-direction.

In summary, in the case of soft and weak inclusions (bottom left corner) the cracks initiate in the inclusions and in the situation of stiff and strong inclusions (top right corner) the cracking occurs only in the matrix region, as expected. Also, the results for a homogeneous material in stiffness agree with intuition. However, the intermediate cases involving soft and strong or stiff and weak inclusion cases have competing effects and the results are somewhat less intuitive as they are sensitive to the combination of two parameters investigated.

We may add at this point that we have chosen as a second parameter the ratio $\varepsilon^i_{cr}/\varepsilon^m_{cr}$. Alternatively, we could choose the ratio of stress strengths $\sigma^i_{cr}/\sigma^m_{cr}$ or the ratio of elastic strain energies U^i_{cr}/U^m_{cr}. Had we chosen $\sigma^i_{cr}/\sigma^m_{cr}$ as the second parameter instead of $\varepsilon^i_{cr}/\varepsilon^m_{cr}$, then the definition of weak vs strong may be affected. For example, when $C^i/C^m = 10$ and $\varepsilon^i_{cr}/\varepsilon^m_{cr} = 0.1$ then $\sigma^i_{cr}/\sigma^m_{cr} = C^i/C^m \cdot \varepsilon^i_{cr}/\varepsilon^m_{cr} = 1$. Thus, the inclusion 10 times weaker in strain strength has the same stress strength as the matrix. Therefore, it is weak in terms of the strain strength, but not the stress strength. Similarly, the case $C^i/C^m = 0.1$ and $\varepsilon^i_{cr}/\varepsilon^m_{cr} = 10$ gives the stress strength ratio $\sigma^i_{cr}/\sigma^m_{cr} = 1$. Therefore, it is strong in terms of the strain strength, but has the same stress strength as the matrix. Our choice was based on the fact that in our numerical simulations we expressed the fracture criterion in terms of strain strengths [eqn (7)]; this is discussed in more detail in Section 3.2.

Figure 6 gives stress–strain curves in the damage map for the realizations shown in Figs 4 and 5. Recall that we assumed that both constituents of the composite, the matrix and inclusions, are elastic–brittle in response. Interestingly, we obtain three distinct types of macroscopic stress–strain curves: (a) elastic–brittle; (b) pre-peak (when a "dip" in stress–strain curve occurs prior to reaching maximum stress strength); and (c) post-peak (when a "dip" in stress–strain curves occurs after the maximum stress strength was reached), as shown in Fig. 3. This observation about these two additional types of stress–strain responses was made by Ostoja-Starzewski *et al.* (1994a, 1997).

In Fig. 6 we observe the pre-peak response in two cases, $C^i/C^m = 0.1$ and 1, when $\varepsilon^i_{cr}/\varepsilon^m_{cr} = 0.1$. For these two parameter combinations there is extensive cracking in inclusions prior to the final failure. This gives a toughening effect and thus the pre-peak type of response. Note that the sharp dip in the early portion of the stress–strain curve for the case $C^i/C^m = 1$, $\varepsilon^i_{cr}/\varepsilon^m_{cr} = 0.1$ corresponds to the point when all inclusions fracture simultaneously (since the stress is uniform but their strength is lower).

The remaining effective stress–strain curves are of either post-peak or elastic brittle type. These occur when damage is matrix dominated, i.e. only matrix bonds break. When

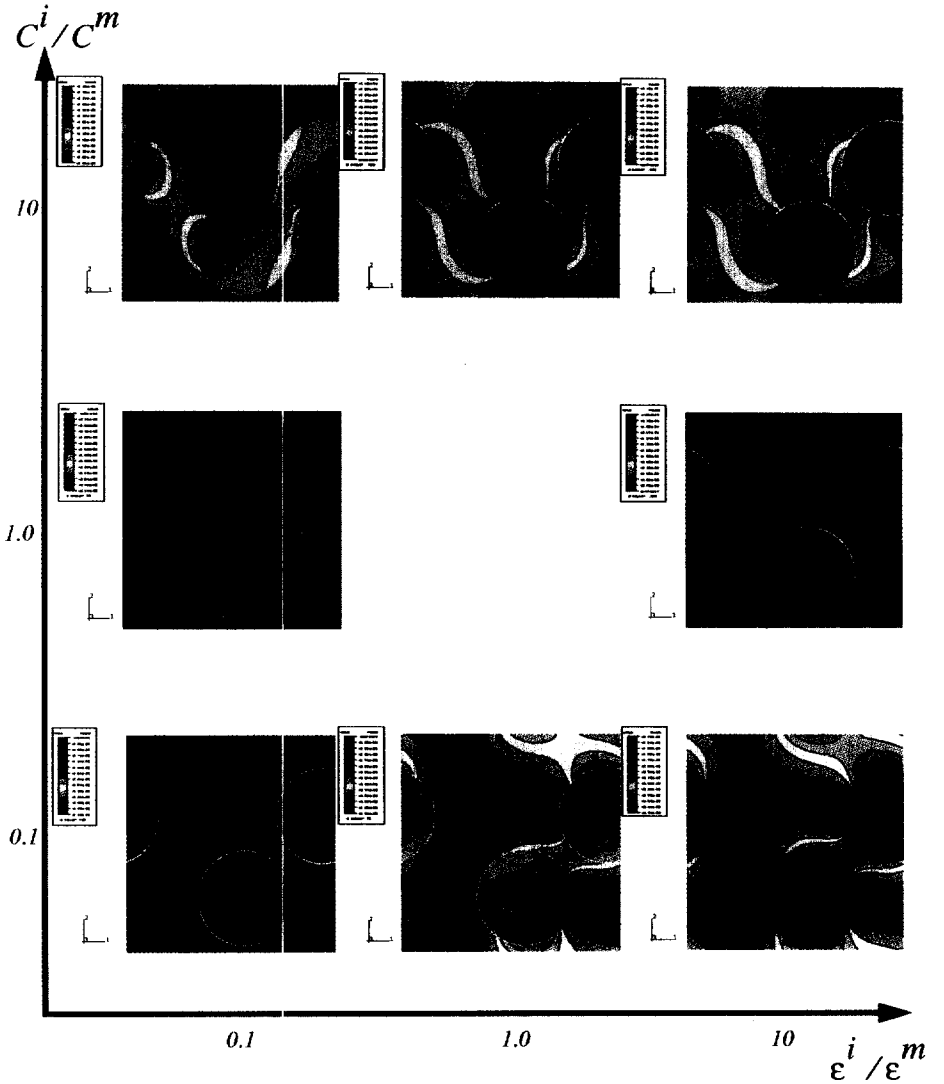

Fig. 4. Strain contours $\varepsilon_{13}/\varepsilon_{cr}$ in the damage plane for scale $\delta = 31/14 = 2.2$.

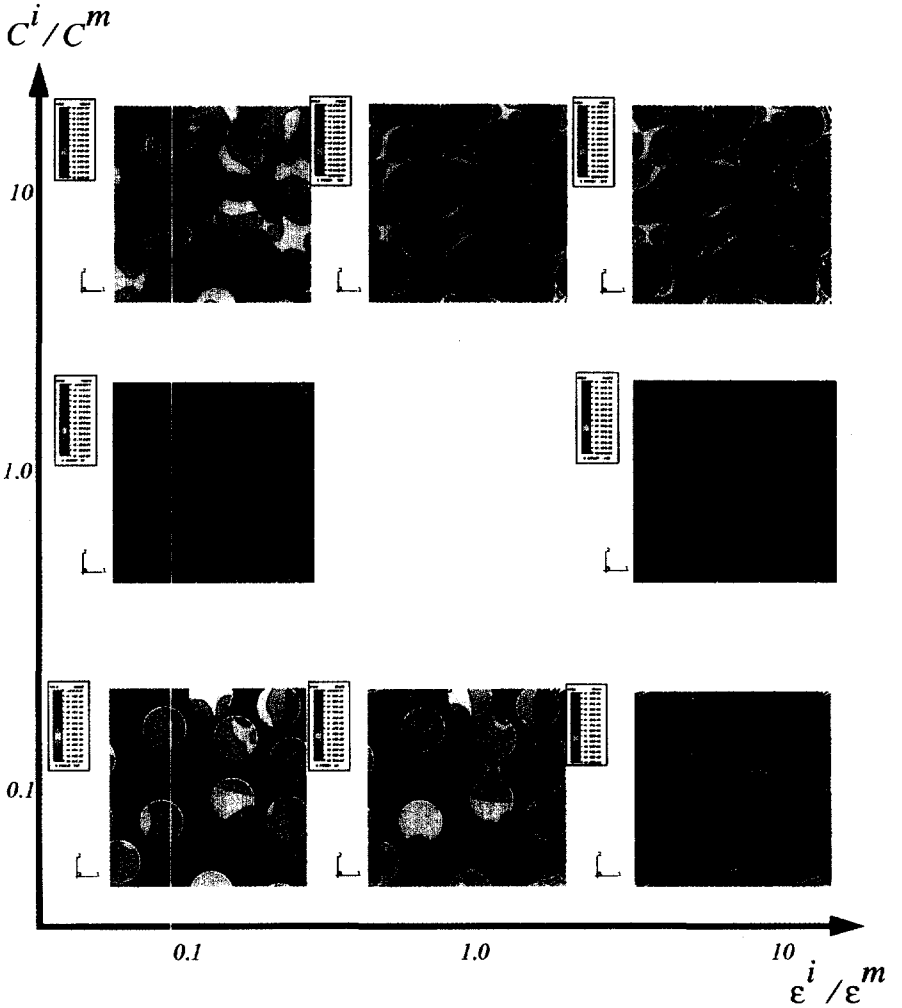

Fig. 7. Strain contours $\varepsilon_{13}/\varepsilon_{cr}$ in the damage plane for scale $\delta = 63/14 = 4.5$.

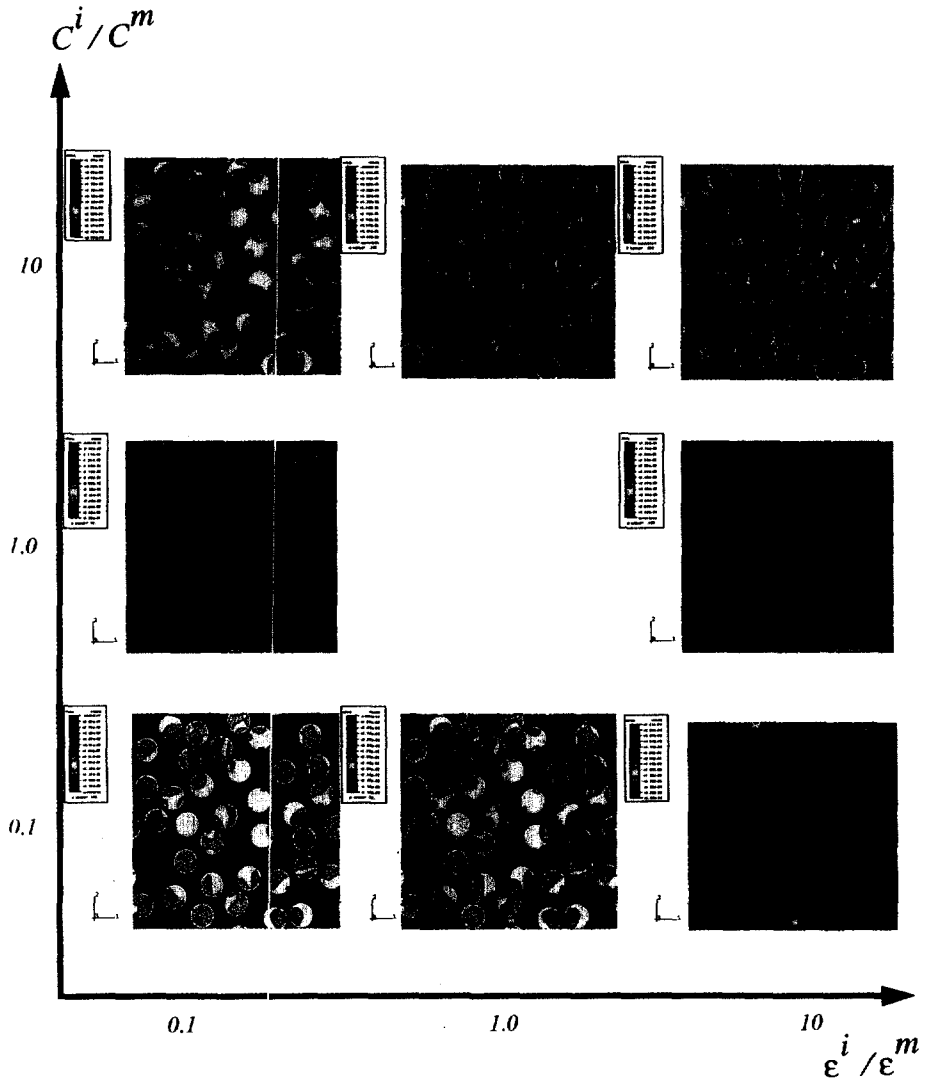

Fig. 10. Strain contours $\varepsilon_{13}/\varepsilon_{cr}$ in the damage plane for scale $\delta = 127/14 = 9.1$.

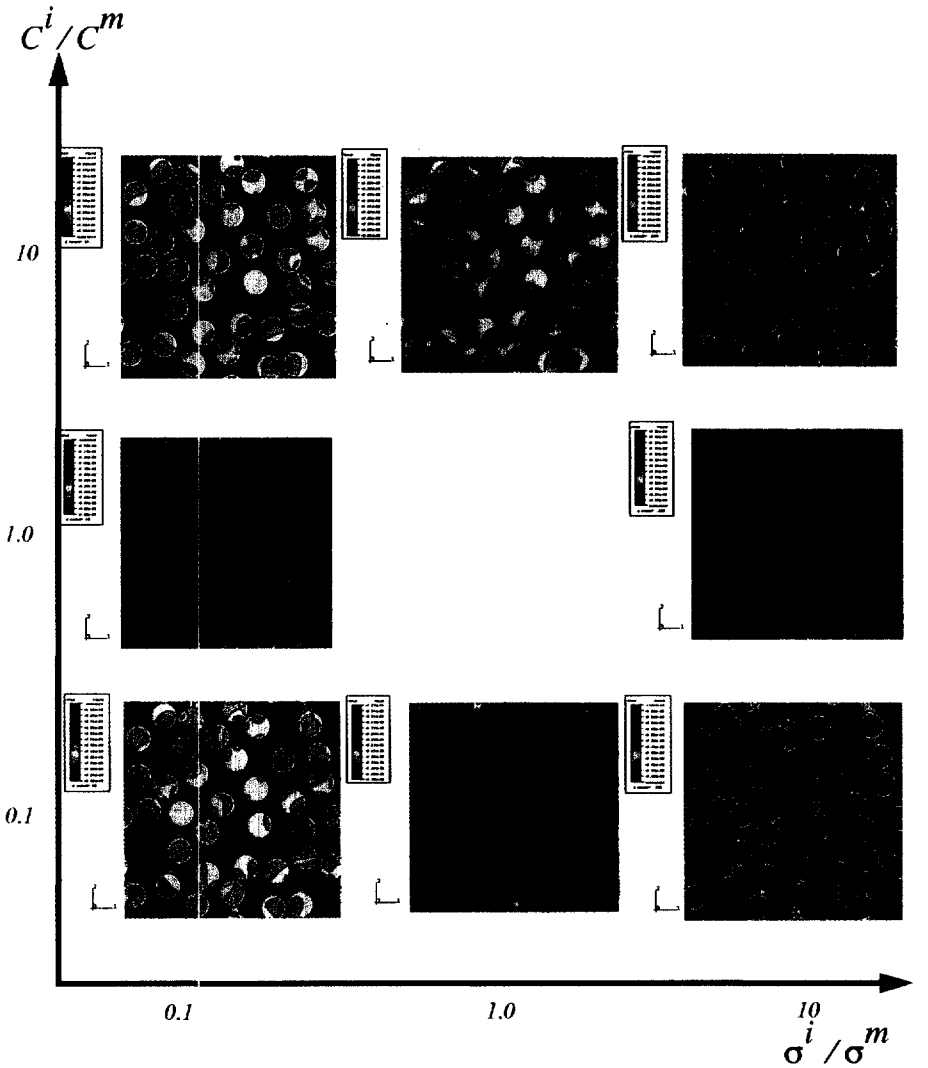

Fig. 13. Strain contours $\varepsilon_{13}/\varepsilon_{cr}$ in the stress–damage plane for scale $\delta = 127/14 = 9.1$ for the same realization as in Fig. 10.

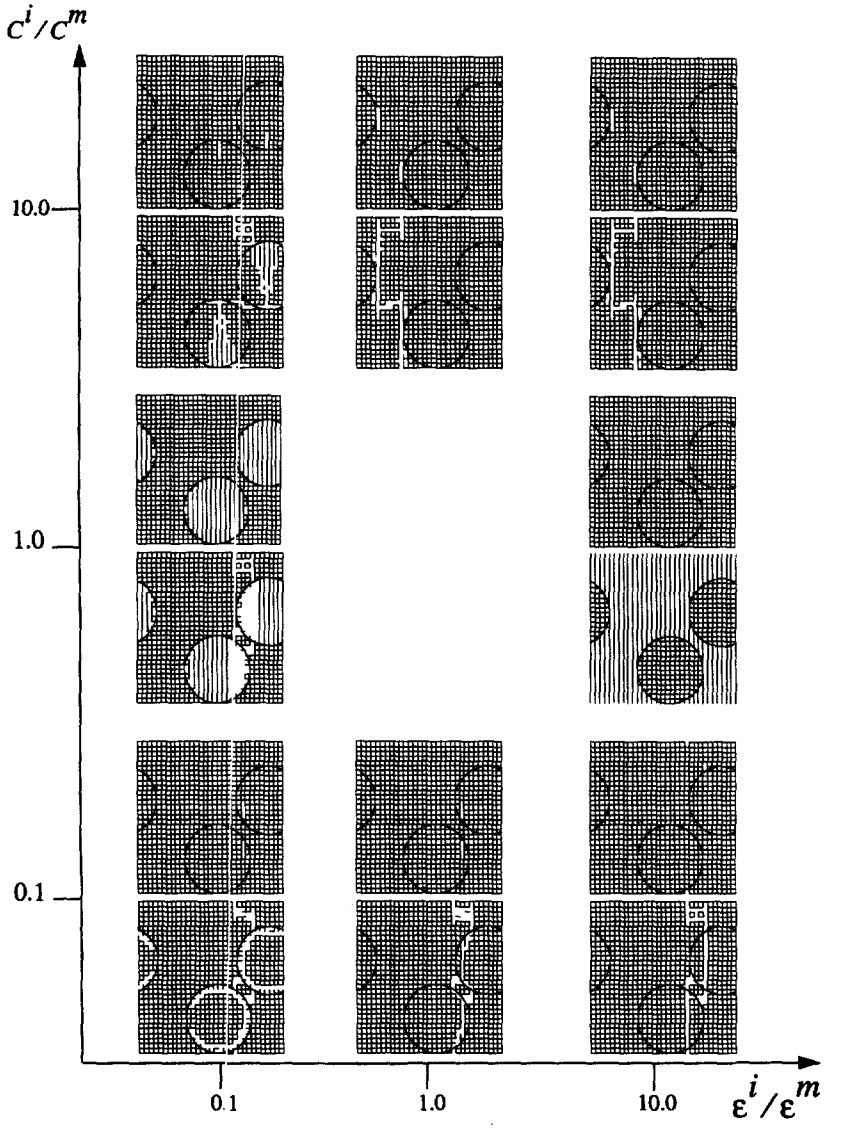

Fig. 5. Crack patterns in the damage plane for scale $\delta = 31/14 = 2.2$ for the same realization as in Fig. 4.

$C^i/C^m = 1$, $\varepsilon^i_{cr}/\varepsilon^m_{cr} = 1$ as well as 10, we have elastic–brittle response, as expected. A similar case is true when $C^i/C^m = 10$, $\varepsilon^i_{cr}/\varepsilon^m_{cr} \geqslant 1$. Note that, $C^i/C^m = 1$, $\varepsilon^i_{cr}/\varepsilon^m_{cr} = 1$ is the trivial case of a homogeneous material.

Thus, as we move in the damage plane from the left to the right and from the bottom to the top, the macroscopic stress–strain responses change from the pre-peak type (due to the inclusion dominated damage) to post-peak or elastic–brittle types.

Figure 8 gives crack/damage patterns for the intermediate window size $\delta = 4.5$. Here, due to the space constraint we only show the final crack patterns. Note that the damage patterns display very similar trends as in the $\delta = 2.2$ case, but they must differ in local details due to different geometric arrangements in both windows. Thus, again the cases of $\varepsilon^i_{cr}/\varepsilon^m_{cr} = 0.1$ with $C^i/C^m = 0.1$ and 1 show the extensive damage in the inclusions prior to the final failure (this is expected since inclusions are softer and weaker than the matrix). The cases $C^i/C^m = 0.1$ with $\varepsilon^i_{cr}/\varepsilon^m_{cr} = 10$ and $C^i/C^m = 10$ with $\varepsilon^i_{cr}/\varepsilon^m_{cr} = 0.1$ show damage in both the inclusions and the matrix. These are transitional cases with both matrix inclusions undergoing cracking due to the competing effects of two parameters. Finally, in the cases $C^i/C^m = 1$, $\varepsilon^i_{cr}/\varepsilon^m_{cr} = 10$ and $C^i/C^m = 10$, $\varepsilon^i_{cr}/\varepsilon^m_{cr} \geqslant 1$ the damage is solely in the matrix. Also,

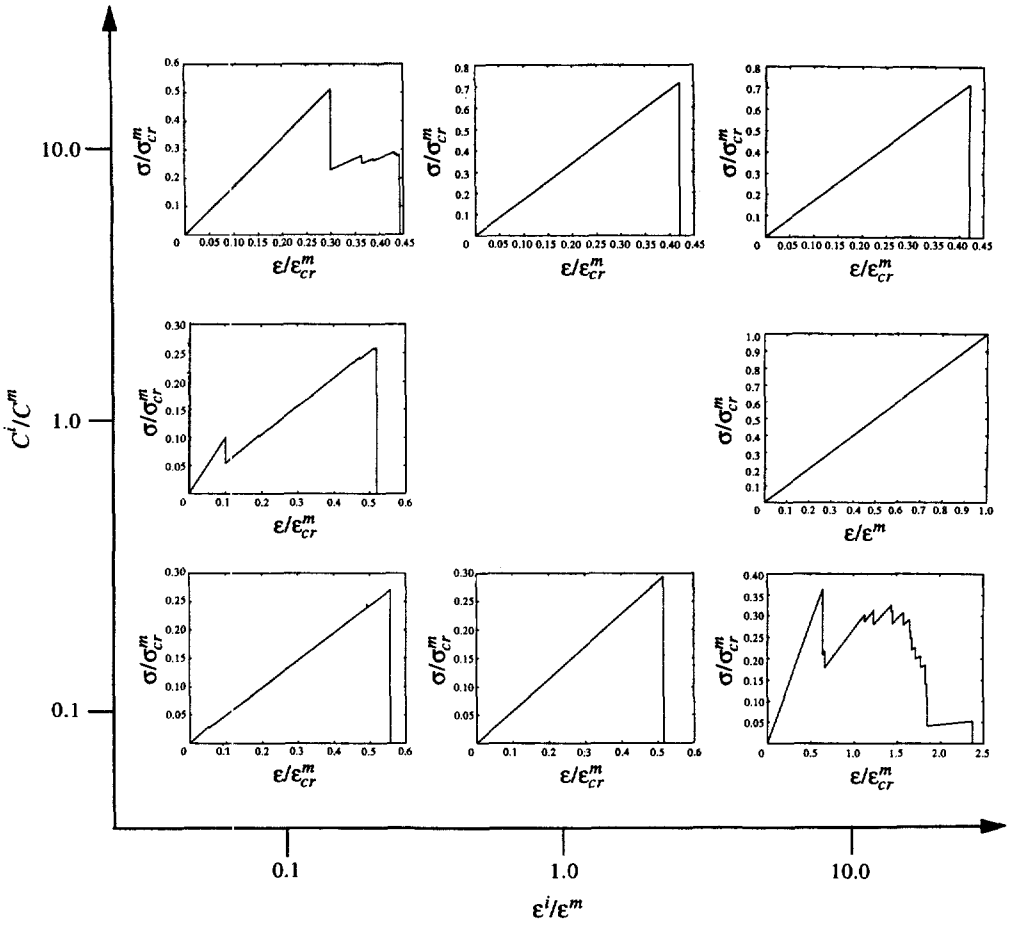

Fig. 6. Effective stress–strain curves in the damage plane for scale $\delta = 31/14 = 2.2$ for the same realization as in Fig. 4.

the last two cases have identical crack patterns as in Fig. 5 even though $\varepsilon^i_{cr}/\varepsilon^m_{cr}$ changed from 1 to 10, this is due to the fact that damage occurs solely in the matrix. Again, the strain contours given in Fig. 7 confirm the locations of dominant crack patterns.

The macroscopic stress–strain patterns for the realization given in Figs 7–8 are shown in Fig. 9. The trend is generally similar to that of the smaller window size (Figs 4–6), although two differences are present: the case $C^i/C^m = 0.1$ with $\varepsilon^i_{cr}/\varepsilon^m_{cr} = 10$ is pre-peak while $C^i/C^m = 10$ with $\varepsilon^i_{cr}/\varepsilon^m_{cr} = 0.1$ is of elastic–brittle type as opposed to post-peak type for corresponding cases in Fig. 6. These differences are not only due to a difference in the window size, but to a fact that configurations on different scales must necessarily be different. In addition, these two cases are transitional ones with two competing effects, soft and strong inclusions in a stiff and weak matrix, or vice versa. For example, if we considered more realizations for the first case, we would find both types of responses as illustrated in Fig. 16.

Figures 10–12, representing the $\delta = 9.1$ case, resemble qualitatively the $\delta = 2.2$ and 4.5 scales given by Figs 4–6 and 7–9. The crack patterns, shown in Fig. 11, obey the same trends as the two smaller window sizes with the damage patterns changing from being inclusion dominated as we move from the left to the right and from the bottom to the top in the damage map. Correspondingly, the stress–strain curves change from pre-peak to elastic–brittle (or post peak) as we move in the damage planes in those directions, as shown in Fig. 12. The character of strain pattern in Fig. 10 is very close to that of Fig. 7, showing the same trends for all parameter combinations; of course, the four times larger number of disks begins to look like a realistic composite. Also, the cases of high stiffness ratio in the

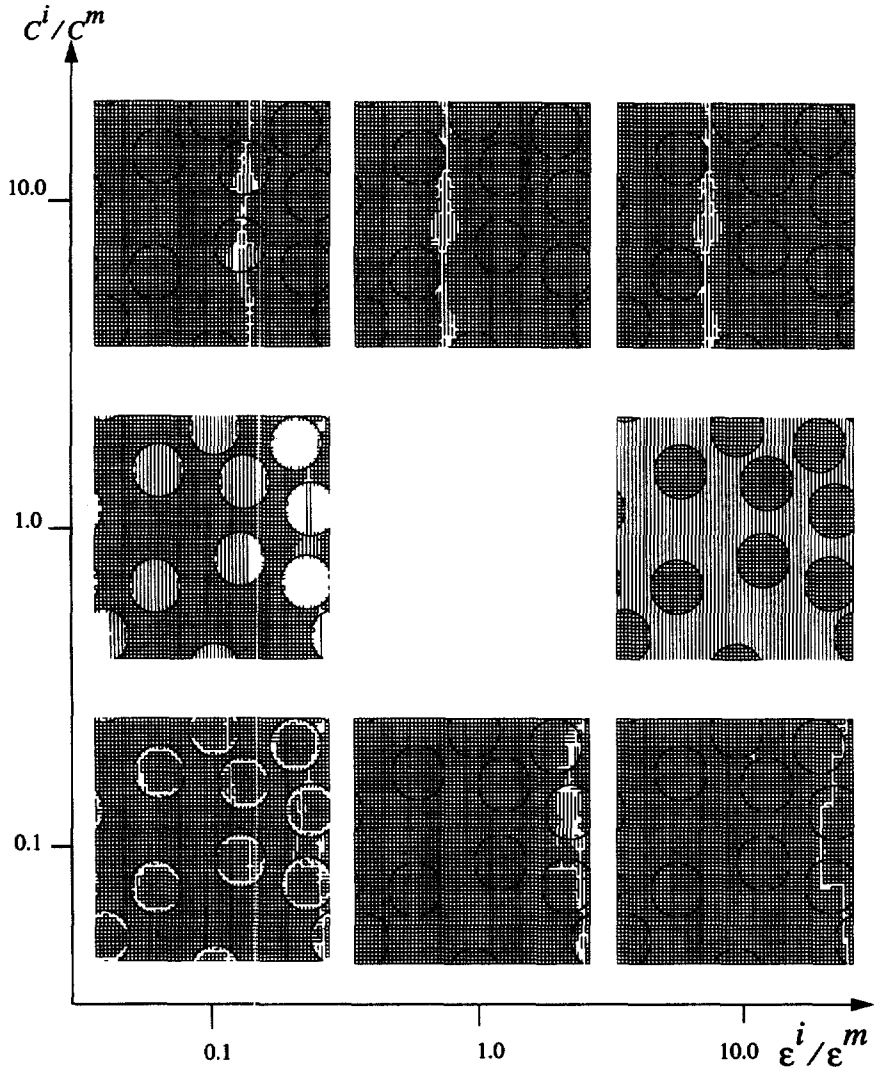

Fig. 8. Crack patterns in the damage plane for scale $\delta = 63/14 = 4.5$ for the same realization as in Fig. 7.

top row of Fig. 10 display "trees" of inclusions carrying the load, which are analogous to trees of grains in a granular matter (Shen *et al.*, 1992), although in the latter case the stiffness of the matrix phase is zero and the grain–grain contacts are direct.

Finally, it is interesting to note that the largest toughening effect is exhibited by a composite with soft inclusions with high strain strength (i.e. easily deformable). This situation may correspond, for example, to a composite having rubber-like (but elastic–brittle) inclusions in an epoxy matrix.

3.2. *Interpretation in terms of stress strengths*

All the preceding results were given in terms of the effective stiffness ratio C^i/C^m and the strain strength ratio $\varepsilon^i_{cr}/\varepsilon^m_{cr}$. Classically, however, strength is perceived in terms of stresses, and so we can set up a damage plane with C^i/C^m and $\sigma^i_{cr}/\sigma^m_{cr}$, whereby it is readily established that $\sigma^i_{cr}/\sigma^m_{cr} = C^i/C^m \cdot \varepsilon^i_{cr}/\varepsilon^m_{cr}$. It follows that, in order to cover the range of stress strengths 0.1, 1.0 and 10.0, for $C^i/C^m = 0.1$, 1.0 and 10.0, we have to shift the top row of the previously discussed damage maps by one column to the right and the bottom row by one column to the left, this corresponds to a "square-rhomb" transformation in going from the $\varepsilon^i_{cr}/\varepsilon^m_{cr}$ parametrization to a $\sigma^i_{cr}/\sigma^m_{cr}$ parametrization. Thus, two corner cases need to be added:

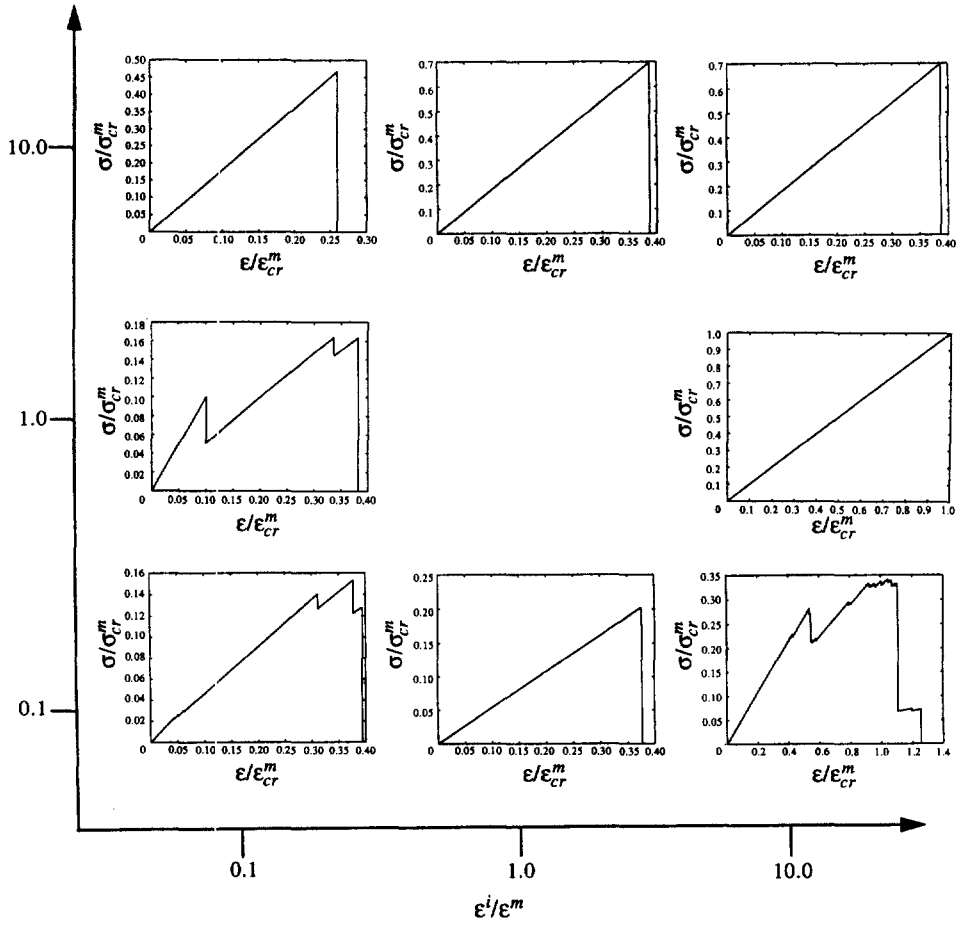

Fig. 9. Effective stress–strain curves in the damage plane for scale $\delta = 63/14 = 4.5$ for the same realization as in Fig. 7.

$\sigma^{i}_{cr}/\sigma^{m}_{cr} = 0.1$ for $C^{i}/C^{m} = 10.0$ in the upper left corner, and $\sigma^{i}_{cr}/\sigma^{m}_{cr} = 10.0$ for $C^{i}/C^{m} = 0.1$ in the lower right corner.

These newly added corner cases are shown, together with the other ones known from the preceding section, in a sequence of plots Figs 13–15 for $\delta = 9.1$. The first of these gives the state of strain contours normalized by the local critical strain in the given phase, whereby the warmer the color the closer is the material to its ε_{cr}. Thus, the yellow/orange coloring of inclusions in the top left corner indicates that they are closer to failure than the matrix, which is confirmed by Fig. 14. Indeed, damage occurs in the inclusions and is finalized by cracks bridging through the matrix. The phenomenon is accompanied by a plateau of toughening in the effective stress–strain curve of Fig. 15, which is then followed by a soft modulus slope of the already weakened matrix.

On the other hand, the newly added lower left hand corner case shows an opposite kind of competition: as shown in Fig. 13, strains in the matrix necks between the contiguous inclusions are highest. Thus, in Fig. 14 we observe a little spatially distributed damage culminating by a crack percolating through these weakest neck regions. Finally, as Fig. 15 shows, this is accompanied by some pre-peak damage and a considerable range of post-peak damage.

4. STATISTICS OF EFFECTIVE MODULI AND STRENGTHS

The discussion so far was concerned with the response of a single geometric configuration for each of the three window sizes. The next question that we ask is: how will the stress–strain curves differ as we change the geometric arrangements, but keep identical

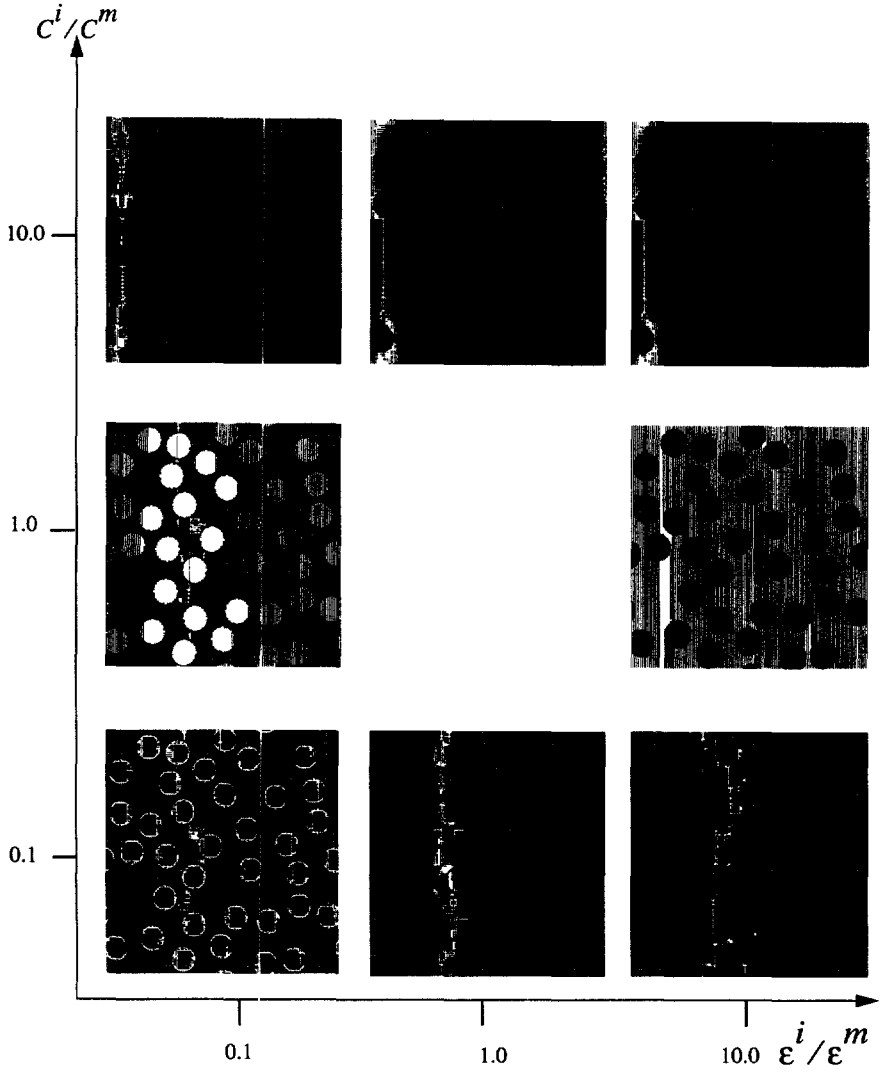

Fig. 11. Crack patterns in the damage plane for scale $\delta = 127/14 = 9.1$ for the same realization as in Fig. 10.

volume fractions and parameter combinations? To illustrate this point we show in Fig. 16 the damage map for $\delta = 4.5$ showing 20 realizations of stress–strain curves. First, we observe that the scatter is rather small in C^{eff}, but considerably larger in $\sigma_{\max}$ and $\varepsilon_{\max}$. The stress–strain responses obey similar trends as for a single realization. Namely, the cases $C^i/C^m = 0.1$, $\varepsilon^i_{cr}/\varepsilon^m_{cr} = 0.1$ and 1 have pre-peak type response. The dip in the case of $C^i/C^m = 1$ and $\varepsilon^i_{cr}/\varepsilon^m_{cr} = 0.1$ occurs at the same strain for all realizations; this corresponds to a simultaneous damage in all the inclusions. The cases when $C^i/C^m = 10$, $\varepsilon^i_{cr}/\varepsilon^m_{cr} = 0.1$, 1.0, 10 and $C^i/C^m = 1$, $\varepsilon^i_{cr}/\varepsilon^m_{cr} = 10$ are elastic–brittle (or post-peak responses in just a few cases), while the cases of $C^i/C^m = 0.1$, $\varepsilon^i_{cr}/\varepsilon^m_{cr} = 1.0$, 10 are alternating between pre-peak and post-peak responses. This illustrates the competing effect of two parameters with both inclusions and the matrix undergoing damage processes.

Random scatter in constitutive response of a disordered composite, hinted at in the foregoing discussion, must be accompanied by a common feature: the scale dependence. Therefore, we now discuss the statistics of two primary quantities of interest, namely C^{eff} and $\sigma_{\max}$, as functions of δ. In such a study the question to ask is: how many realizations do we need for each window size? Since it is known that scatter is highest at smallest scales, that is for $\delta = 2.2$, we take 1000 realizations for each parameter combination; at $\delta = 4.5$ we run 100 configurations, while at $\delta = 9.1$, 40 configurations (see also Table 1). The

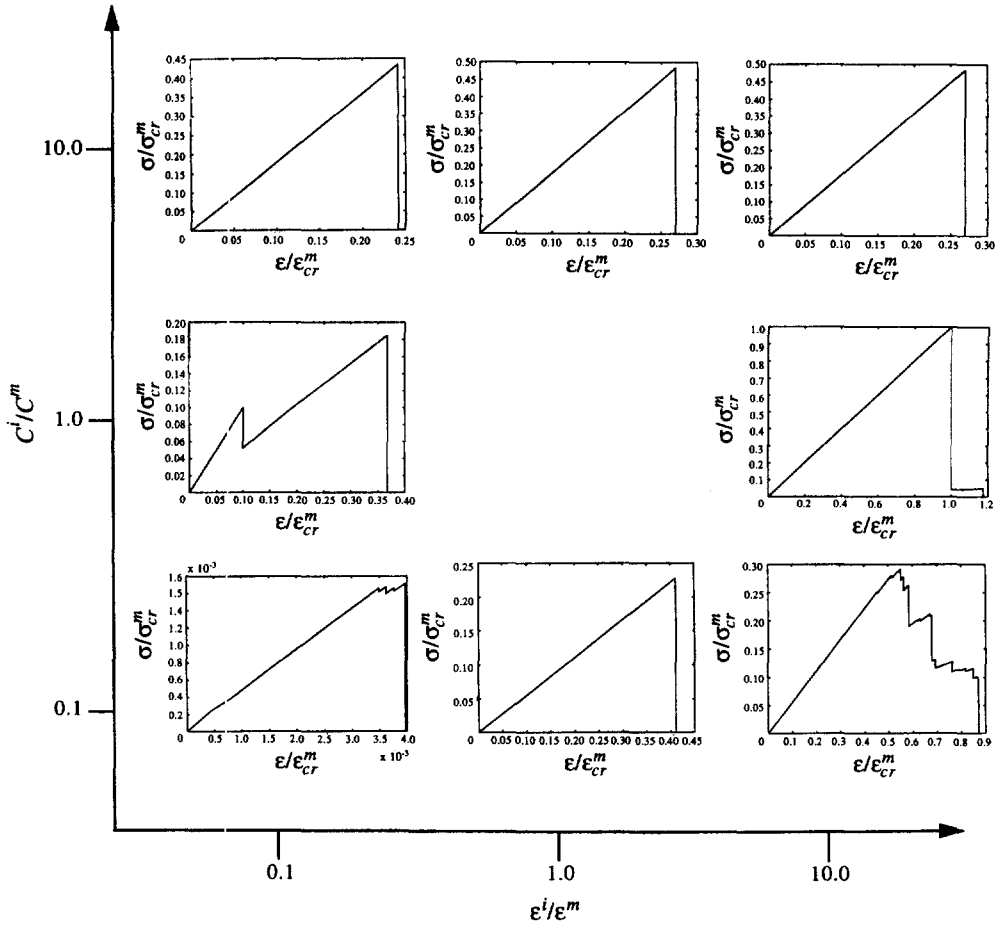

Fig. 12. Effective stress–strain curves in the damage plane for scale $\delta = 127/14 = 9.1$ for the same realization as in Fig. 10.

smaller number of realizations $\mathbf{B}_\delta(\omega)$ for larger window size is, of course, a welcome aspect of the problem given the fact that computational times grow with δ increasing.

The numbers of samples in Table 1 are also justified by plots of the coefficients of variation (ratios of the standard deviation to the mean) of C^{eff} and $\sigma_{\max}$ as functions of the number of realizations n (from 1 to 1000). Selected cases are given in Fig. 17. First, Fig. 17(a) gives a plot of coefficient of variation (COV) of C^{eff} for a window size $\delta = 2.2$ vs the number of realizations n (from 1 to 1000). Note the significant scatter for the number of realizations in the double digits and its subsequent decay. Similar curves, but for the maximum strength $\sigma_{\max}$ are given in Fig. 17(b) for $\delta = 2.2$, and in Fig. 17(c) for $\delta = 4.5$. Clearly, a smaller number of realizations is needed for $\delta = 4.5$ and $n = 100$ is quite sufficient to represent the data as the response exhibits only small order fluctuations when n is close to 100.

In Tables 2–3 we summarize the effect of two parameters C^i/C^m and $\varepsilon^i_{cr}/\varepsilon^m_{cr}$ and the window size on the mean and the coefficient of variation on C^{eff} and $\sigma_{\max}$, respectively. The following observations can be made about C^{eff}. First of all, observe that the statistics of C^{eff} are not influenced by $\varepsilon^i_{cr}/\varepsilon^m_{cr}$, as expected, that is the results in each row, i.e. for C^i/C^m fixed for $\varepsilon^i_{cr}/\varepsilon^m_{cr} = 0.1$, 1, 10, are identical for each window size. Secondly, the scatter depends weakly on parameters C^i/C^m and the scatter in C^{eff} is slightly higher when $C^i/C^m = 10$ than when $C^i/C^m = 0.1$. When $C^i/C^m = 1$, the effective stiffness is identically a unity and no scatter exists. Finally, the scatter decreases as the window size increases, i.e. for example when $C^i/C^m = 10$, the COV is 4.4% for $\delta = 2.2$, 1.6% for $\delta = 4.5$, and 0.6% for $\delta = 9.1$, and similar values are for $C^i/C^m = 0.1$.

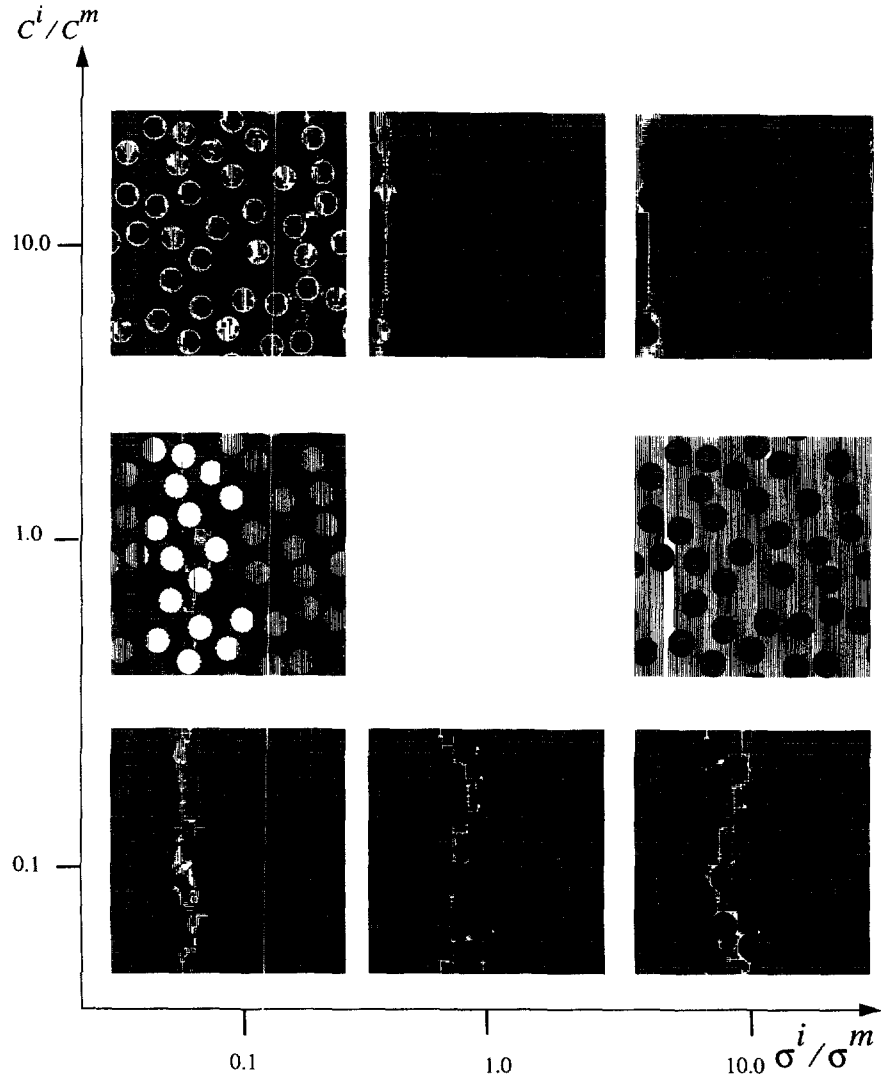

Fig. 14. Crack patterns in the stress–damage plane for scale $\delta = 127/14 = 9.1$ for the same realization as in Fig. 10.

Similarly, the results for the coefficient of variation of σ_{max} are given in Table 4. First of all, when $C^i/C^m = 1$ and $\varepsilon^i_{cr}/\varepsilon^m_{cr} \geqslant 1$ there is no scatter in responses. This is expected because in these situations the stress fields are uniform and the whole matrix cracks simultaneously. However, the scatter in response exists for all the remaining cases, including the case when $C^i/C^m = 1$ and $\varepsilon^i_{cr}/\varepsilon^m_{cr} = 0.1$. Note that the coefficient of variation of σ_{max} is very strongly dependent on C^i/C^m and $\varepsilon^i_{cr}/\varepsilon^m_{cr}$ and the highest scatter is when $C^i/C^m = 0.1$ and $\varepsilon^i_{cr}/\varepsilon^m_{cr} = 0.1$, i.e. when inclusions are soft and weak (20.2% for $\delta = 2.2$ and 13.4% for $\delta = 4.5$).

A similar type of scatter is present in the case $C^i/C^m = 1$ and $\varepsilon^i_{cr}/\varepsilon^m_{cr} = 0.1$ (19.1% for $\delta = 2.2$ and 12.6% for $\delta = 4.5$). When $C^i/C^m = 0.1$ and $\varepsilon^i_{cr}/\varepsilon^m_{cr}$ is increasing from 0.1, 1 to 10, the scatter is decreasing as 20.2, 14.1 and 8.4% for $\delta = 2.2$ and 13.4, 9.6 and 4.7% for $\delta = 4.5$. When $C^i/C^m = 10$ the fluctuations are smaller as $\varepsilon^i_{cr}/\varepsilon^m_{cr}$ is changing and now the case of stiff and strong inclusions gives higher values, i.e. the scatter increases as $\varepsilon^i_{cr}/\varepsilon^m_{cr}$ increases. This is opposite to the response in the bottom row. Thus, as we move in the damage (parameter) plane in the top row ($C^i/C^m = 10$) scatter increases as we move to the right, i.e. $\varepsilon^i_{cr}/\varepsilon^m_{cr}$ increases, while in the bottom row ($C^i/C^m = 0.1$) the scatter decreases as $\varepsilon^i_{cr}/\varepsilon^m_{cr}$ increases. If we consider the first column, where $\varepsilon^i_{cr}/\varepsilon^m_{cr} = 0.1$ and C^i/C^m is changing, the COV decreases as C^i/C^m increases, whereas for $\varepsilon^i_{cr}/\varepsilon^m_{cr} = 1$ the scatter is higher for the

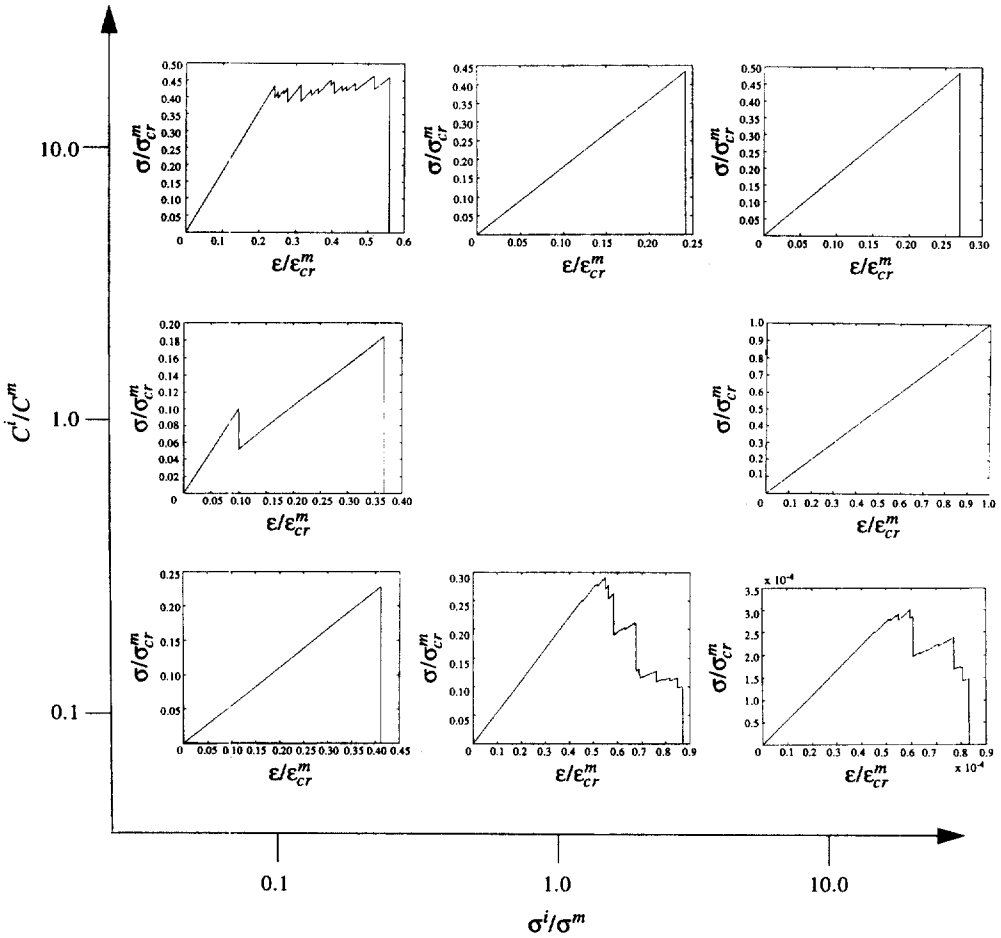

Fig. 15. Effective stress–strain curves in the stress–damage plane for scale $\delta = 127/14 = 9.1$ for the same realization as in Fig. 10.

$C^i/C^m = 0.1$ case than for $C^i/C^m = 10$, and finally when $\varepsilon^i_{cr}/\varepsilon^m_{cr} = 10$ that scatter is higher when $C^i/C^m = 10$. Finally, note that in general the scatter decreases as the window size increases, similarly as for C^{eff}. This trend holds for all the cases except when $\delta = 2.2$ and $C^i/C^m = 10$. This may be due to the fact that $\delta = 2.2$ is too small and because we use periodic boundary conditions. However, the correct trend exists as we inspect $\delta = 4.5$ and 9.1 window sizes.

The important question to pose now is: what probability distribution function will give best fit for this data? To address this issue we consider up to 10 possible candidates for such functions: beta, Gauss, Gumbel Min, Rayleigh, Weibull, χ, χ^2, etc. (see the Appendix). We then use a Kolmogorov–Smirnov test and a Chi-square test to determine the top candidates for each combination of parameters and three window sizes. As might be expected, the results of these two tests are typically at odds with one another. Moreover, no single probability distribution is found to be optimal for the entire range of parameters in the damage plane. However, the beta function can be proposed as a most universal fit overall for C^{eff} as well as σ_{max}. This is due to two facts: firstly, beta involves four free parameters as opposed to two or three as is the case with other functions. Secondly, it has finite limits unlike other functions, and both quantities are definitely restricted to a finite range. First, the quality of the beta fit is shown in Fig. 18 for C^{eff} on logarithmic plots for soft and hard disk systems, as a function of three window sizes. Ostoja-Starzewski (1998) gives a detailed explanation of the usefulness of beta distribution in modeling the flow of probability mass, as a function of δ, from two Dirac deltas weighted by the volume fractions

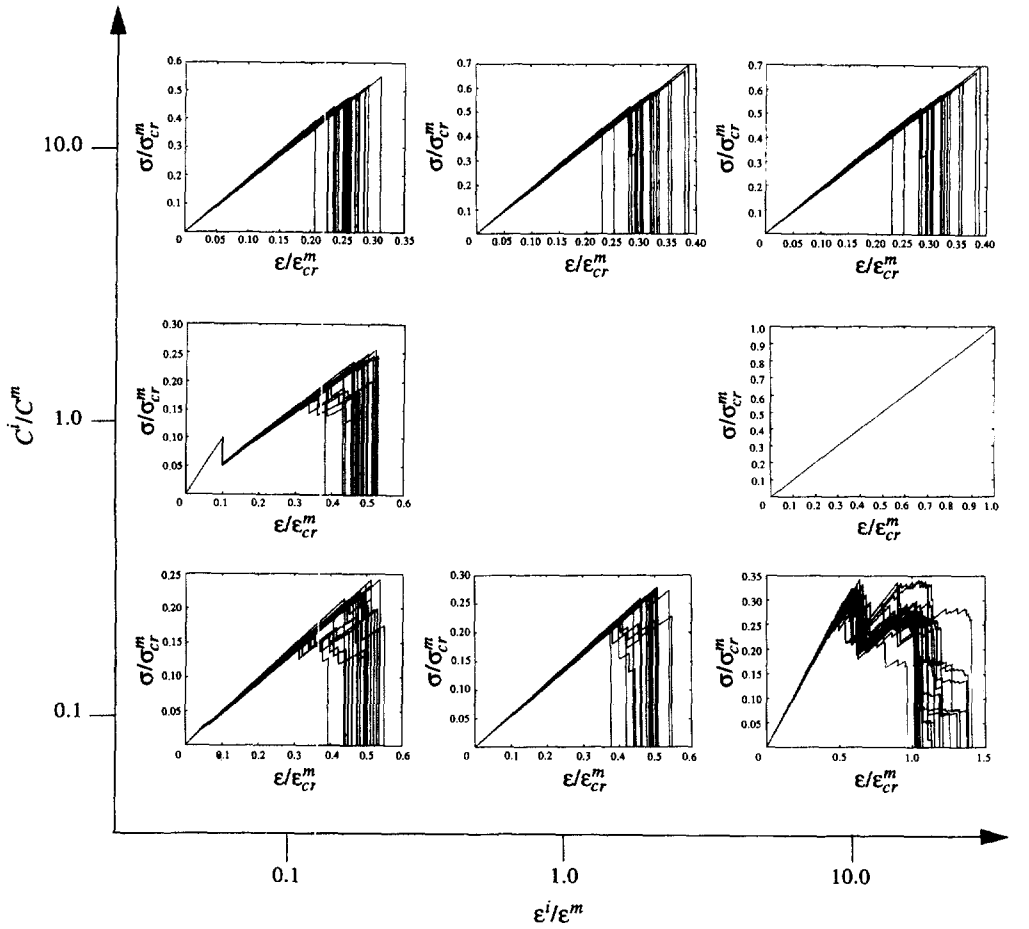

Fig. 16. Damage map of constitutive curves for 20 realizations of the random composite scale $\delta = 63/14 = 4.5$.

Table 1. Three scales and number of realizations simulated

Window size L	Inclusion diameter d	Scale $\delta = L/d$	n
31	14	2.2	1000
63	14	4.5	100
127	14	9.1	40

of both phases towards a single Dirac delta fixed at C^{eff} on a macroscopic scale $\delta \to \infty$. Examples of beta in other composite systems are also presented in that reference.

The sequence of plots in Figs 19–21, all set in the damage plane, give analogous fits of beta for $\sigma_{\max}$. It is important to note here that the commonly used Weibull distribution did not give good fits to our data. This is illustrated in Fig. 22 which gives a typical situation of fits by beta, Gumbel Min, Gauss (i.e. normal), and Weibull to data of $\sigma_{\max}$ for a particular case of C^i/C^m and $\varepsilon_{cr}^i/\varepsilon_{cr}^m$ for $\delta = 4.5$; other cases display very similar trends. While Weibull is worst of these four, it is seen that Gumbel Min and Gauss are perhaps acceptable in a finite range of the data, but beta is best suited for this task. However, given the fact that it is a four parameter function, beta is really at the limits of its capability of modelling a problem governed by four principal material parameters: volume fraction of inclusions, stiffness ratio C^i/C^m, strength ratio $\varepsilon_{cr}^i/\varepsilon_{cr}^m$, and window scale δ. At the same time, its good

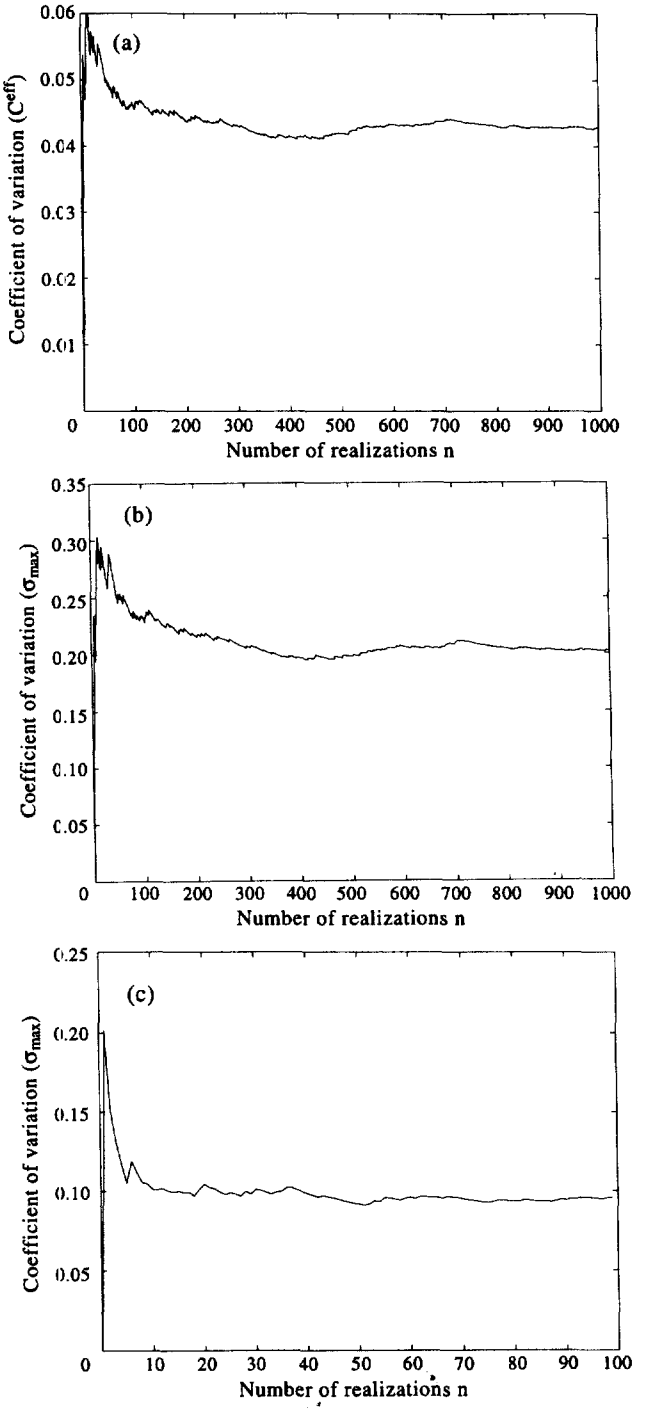

Fig. 17. Graph of the coefficient of variation (COV) versus the number of realizations n for (a) C^{eff} and for (b) σ_{max} when $C^i/C^m = 10$ and $\varepsilon^i_{cr}/\varepsilon^m_{cr} = 0.1$ for $\delta = 31/14 = 2.2$, and for (c) σ_{max} for $\delta = 63/14 = 4.5$ when $C^i/C^m = 10$ and $\varepsilon^i_{cr}/\varepsilon^m_{cr} = 1$.

Table 2. Mean and coefficient of variation (COV) of the effective stiffness C^{eff}

	$C^i/C^m = 0.1$	$C^i/C^m = 10$	
Window	0.578	1.723	mean
size 31	0.043	0.044	COV
Window	0.549	1.814	mean
size 63	0.014	0.016	COV
Window	0.554	1.800	mean
size 127	0.006	0.006	COV

Table 3. Mean values of the maximum stress strength σ_{max}

	$\varepsilon^i/\varepsilon^m = 0.1$	$\varepsilon^i/\varepsilon^m = 1$	$\varepsilon^i/\varepsilon^m = 10$	Window size
$C^i/C^m = 10$	0.537	0.716	0.716	31
	0.478	0.565	0.565	63
	0.434	0.491	0.490	127
$C^i/C^m = 1$	0.293	—	—	31
	0.228	—	—	63
	0.206	—	—	127
$C^i/C^m = 0.1$	0.291	0.325	0.397	31
	0.215	0.260	0.330	63
	0.190	0.237	0.308	127

Table 4. Coefficient of variation of the maximum stress strength σ_{max}

	$\varepsilon^i/\varepsilon^m = 0.1$	$\varepsilon^i/\varepsilon^m = 1$	$\varepsilon^i/\varepsilon^m = 10$	Window size
$C^i/C^m = 10$	0.080	0.084	0.084	31
	0.087	0.119	0.119	63
	0.056	0.079	0.079	127
$C^i/C^m = 1$	0.191	—	—	31
	0.126	—	—	63
	0.072	—	—	127
$C^i/C^m = 0.1$	0.202	0.141	0.084	31
	0.134	0.096	0.047	63
	0.102	0.067	0.043	127

record in reliability theory stands in support of our proposal for its use in a stochastic damage theory; on the latter subject see (Ostoja-Starzewski *et al.* 1997).

5. CONCLUSIONS

(1) Spring network modeling of elastic–brittle responses allows one to rapidly investigate a number of different composite configurations, without a need for remeshing as would be needed with most finite element methods, for a range of various material parameters. Such numerical simulations capture statistical information on geometrical (or materials) variation with much less effort and cost than would be needed in an experimental program; experiments should, of course, be done whenever possible. The simulations were carried out in the setting of periodic boundary conditions for appropriately modified composite microstructures; however, the same approach may be employed for other types of loadings.

(2) Two parameters, stiffness ratio C^i/C^m and strain strength ratio $\varepsilon^i_{cr}/\varepsilon^m_{cr}$, define a so-called damage plane, wherein all combinations of three values 0.1, 1.0 and 10 have been

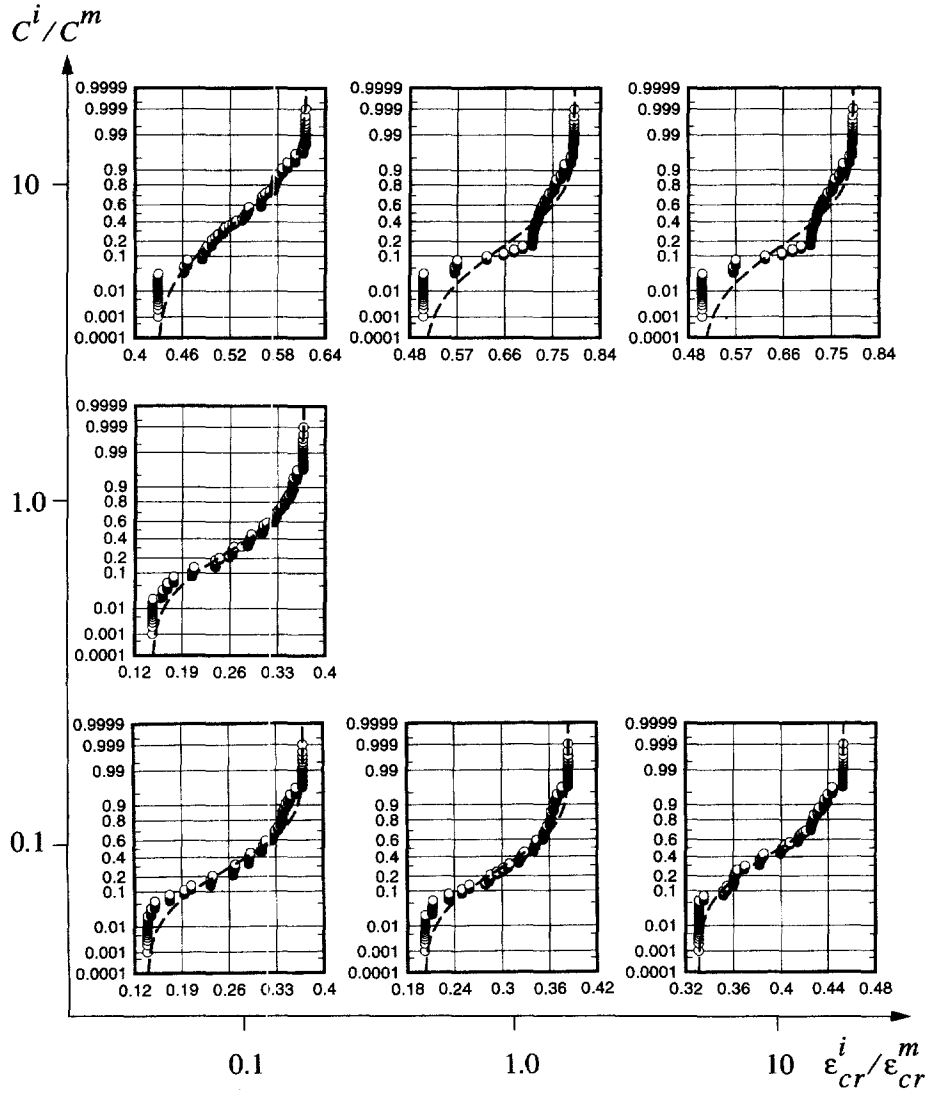

Fig. 19. Probability distribution functions $p(\sigma_{max})$ in the (strain) damage plane for scale $\delta = 2.2$; dots show results of Monte-Carlo runs, curves are the beta fits.

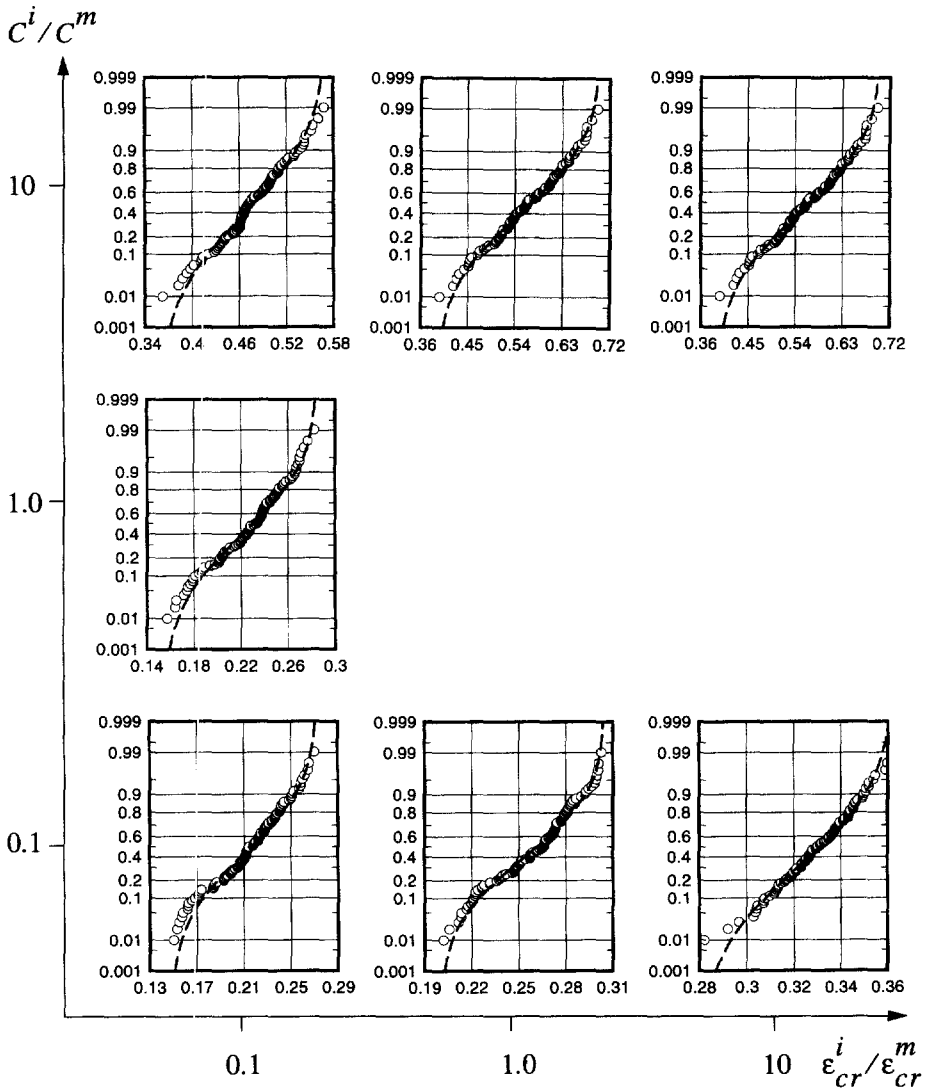

Fig. 20. Probability distribution functions $p(\sigma_{max})$ in the (strain) damage plane for scale $\delta = 4.5$; dots show results of Monte-Carlo runs, curves are the beta fits.

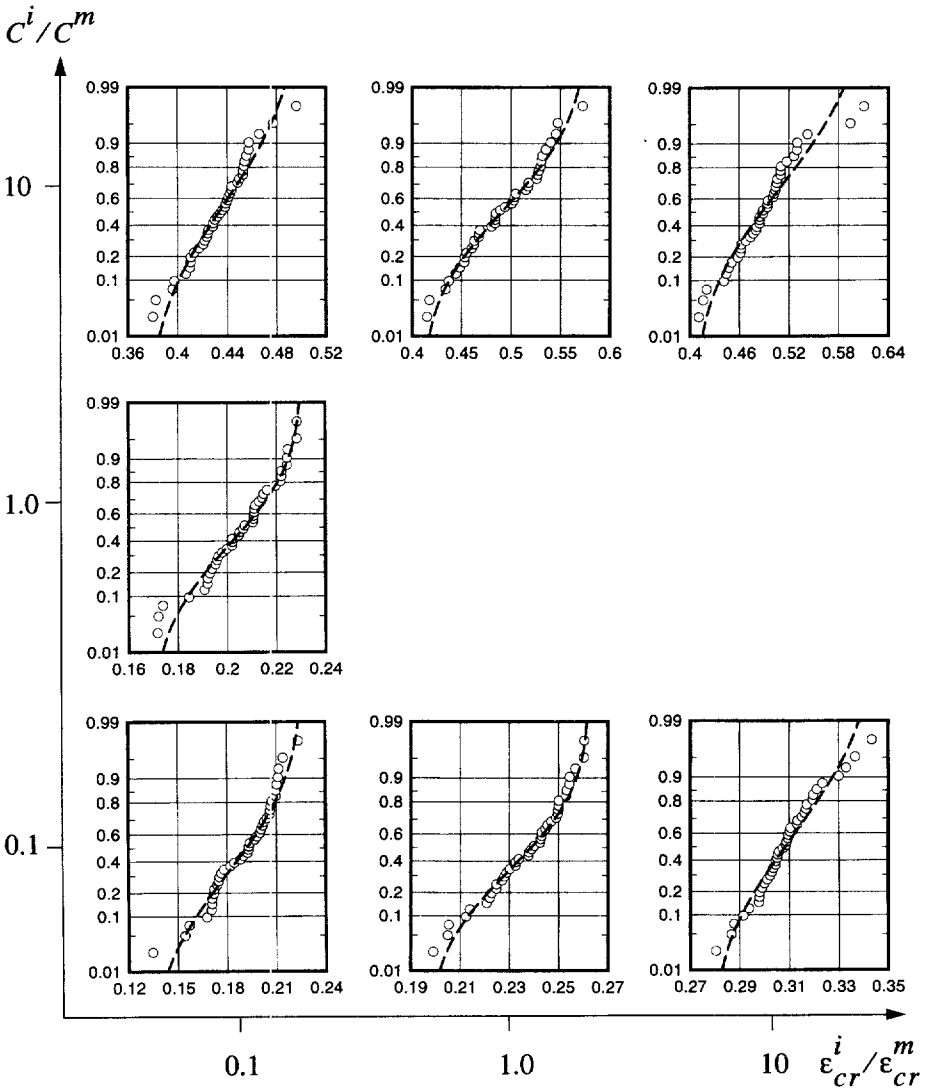

Fig. 21. Probability distribution functions $p(\sigma_{max})$ in the (strain) damage plane for scale $\delta = 9.1$; dots show results of Monte-Carlo runs, curves are the beta fits.

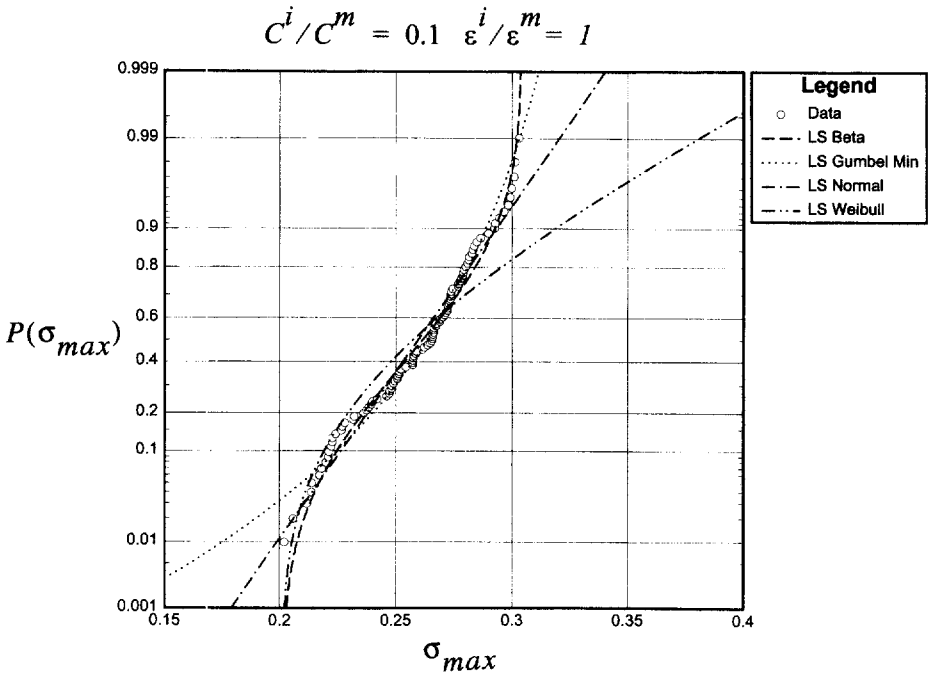

Fig. 22. Fits by beta, Gumbel Min, Gauss (normal), and Weibull distributions to 100 points data of σ_{max} for the case of $C^i/C^m = 0.1$ and $\varepsilon^i_{cr}/\varepsilon^m_{cr} = 1.0$ for scale $d = 4.5$.

inspected numerically to cover a wide range of physically encountered composites for a range of three scales. Three types of effective stress–strain curves have been identified: elastic–brittle, pre-peak and post-peak. These have been explained in terms of various microscale phenomena, such as damage of inclusions, matrix cracking, localized vs spatially distributed damage, etc. Correlations of the damage patterns have been made with the strain fields of the virgin material. Additionally, damage maps have been developed in terms of the stress strength ratio $\sigma^i_{cr}/\sigma^m_{cr}$.

(3) Scatter of the effective constitutive responses has been studied in terms of two quantities: C^{eff} and σ_{max}. The beta distribution has been identified as an optimal probability fit for the entire range of parameters studied in this paper. This result may be useful in setting up of stochastic response laws.

Acknowledgements—This research was supported by the NSF under grants no. MSS 9202772 and MSS 9402285, as well as the Research for Excellence Fund from the State of Michigan.

REFERENCES

Alzebdeh, K., Jasiuk, I. and Ostoja-Starzewski, M. (1998) Scale and boundary conditions effects in damage mechanics of random composites. In *Symposium on Damage Mechanics, McNU'97 Joint ASME–ASCE–SES Summer Conference, Damage Mechanics*, eds J. W. Ju, J.-L. Chaboche and G. Voyiadjis, Chicago (in press).

Baxevanakis, C., Lebon, B. and Renard, J. (1998) Fracture statistics modeling of laminate composites. *International Journal of Solids and Structures* **35**, 2505–2521.

Bazant, Z. P., Bittnar, Z., Jirasek, M. and Mazars, J. (eds) (1994) *Fracture and Damage in Quasi-Brittle Disordered Structures: Experiment, Modelling and Computer Analysis*. E & FN Spon, London.

Beran, M. (1968) *Statistical Continuum Theories*. Interscience, New York.

Breysse, D. (ed.) (1994) *Probabilities and Materials—Tests, Models and Applications*. NATO ASI Series E-269, Kluwer, Dordrecht.

Carpinteri, A. (ed.) (1996) *Size-Scale Effects in the Failure Mechanisms of Materials and Structures*. E & FN Spon, London.

Charmet, J. C., Roux, S. and Guyon, E. (eds) (1990) *Disorder and Fracture*. NATO ASI Series B-235, Plenum Press, New York.

Grah, M., Alzebdeh, K., Sheng, P. Y., Vaudin, M. D., Bowman, K. J. and Ostoja-Starzewski, M. (1996) Brittle intergranular failure in 2D microstructures: experiments and computer simulations. *Acta Materialia* **44**(10), 4003–4018.

Herrmann, H. J. and Roux, S. (eds) (1990) *Statistical Models for the Fracture of Disordered Media*. Elsevier, North-Holland.
Huet, C. (1993) *Micromechanics of Concrete and Cementitious Composites*. Presses Polytech. Univers, Romandes, Lausanne.
Jasiuk, I., Sheng, P. Y. and Ostoja-Starzewski, M. (1994) Influence of random fiber arrangement on crack propagation in brittle–matrix composites. *4th Conference Brittle–Matrix Composites*, eds A. M. Brandt, V. C. Li and I. H. Marshall. Warsaw, Poland, pp. 200–208.
Krajcinovic, D. (1996) *Damage Mechanics*. Elsevier, North-Holland.
Ostoja-Starzewski, M. (ed.) (1997) Statistical fracture mechanics. *Engineering Fracture Mechanics* **57**(2/3), **58**(5/6).
Ostoja-Starzewski, M. (1998) Random field models of heterogeneous materials. *International Journal of Solids and Structures* **35,** 2429–2455.
Ostoja-Starzewski, M. and Lee, J. D. (1996) Damage maps of disordered composites: a spring network approach. *International Journal of Fracture* **75,** R51–R57.
Ostoja-Starzewski, M., Sheng, P. Y. and Jasiuk, I. (1994a) Influence of random geometry on effective properties and damage formation in composite materials. *ASME Journal of Engineering Materials and Technology* **116,** 384–391.
Ostoja-Starzewski, M., Sheng, P. Y. and Jasiuk, I. (1994b) Micromechanics as a basis of stochastic continuum damage mechanics, 1994 ASME Winter Ann. Mtg. In *Material Instabilities: Theory and Applications*, eds R. C. Batra and H. M. Zbib, AMD 183 and MD 50, 131–141.
Ostoja-Starzewski, M., Sheng, P. Y. and Alzebdeh, K. (1996) Spring network models in elasticity and fracture of composites and polycrystals. *Computational Material Science* **7**(1, 2), 82–93.
Ostoja-Starzewski, M., Sheng, P. Y. and Jasiuk, I. (1997) Damage patterns and constitutive response of random matrix–inclusion composites. *Engineering Fracture Mechanics* **58,** 581–606.
Pineau, A. and Zaoui, A. (eds) (1996) *Micromechanics of Plasticity and Damage of Multiphase Materials*. Kluwer, Dordrecht.
Press, W. H., Teukolsky, S. A., Vetterling, W. T. and Flannery, B. P. (1992) *Numerical Recipies*. Cambridge University Press, Cambridge.
Pyrz, R. (ed.) (1995) *IUTAM Symposium on Microstructure–Property Interactions in Composite Materials*. Kluwer, Dordrecht.
Shen, H. H., Satake, M., Mehrabadi, M., Chang, C. S., Campbell, C. S. (eds) (1992) Advances in micromechanics of granular materials. *Stud. Applied Mechanics* **31**.
Sheng, P. Y. (1995) Analytical and computational approaches in mechanics of composite materials. Ph.D. thesis, Michigan State University.
Torquato, S. (1988) Computer simulation results for the two-point probability function of composite media. *Journal of Composite Physics* **76**(1), 176–191.
van Mier, J. G. M. (1996) *Fracture Processes of Concrete: Assessment of Material Parameters for Fracture Models*. CRC Press, Boca Raton.
Weibull, W. (1939) A statistical theory of the strength of materials. *Swedish Royal Institute of Engineering Research* **151,** 1–45.

APPENDIX

For the sake of reference we list here the probability distributions considered in the present study.

Beta

$$f(x;a_1,a_2,\delta_1,\delta_2)=\frac{\left(\frac{x-\delta_1}{\delta_2-\delta_1}\right)^{a_1-1}\left(1-\frac{x-\delta_1}{\delta_2-\delta_1}\right)^{a_2-1}}{(\delta_2-\delta_1)B(a_1,a_2)} \tag{A1}$$

where a_1, a_2, δ_1 and δ_2 are adjustable parameters, and $B(a_1,a_2)=\Gamma(x)\Gamma(y)/(\Gamma(x,y))$ is the beta function.

Gauss (normal)

$$f(x;\mu,\sigma)=\frac{1}{\sqrt{2\pi}\sigma}e^{-\frac{1}{2}\left(\frac{x-\mu}{\sigma}\right)^2} \tag{A2}$$

where μ and σ are adjustable parameters.

Gumbel Min

$$f(x;\mu,\alpha)=\alpha e^{[\alpha(x-\mu)-e^{\alpha(x-\mu)}]} \tag{A3}$$

where μ and α are adjustable parameters.

Rayleigh

$$f(x;\alpha,\varepsilon)=\left(\frac{x-\varepsilon}{\alpha^2}\right)e^{-\frac{1}{2}\left(\frac{x-\varepsilon}{\alpha}\right)^2} \tag{A4}$$

where α and ε are adjustable parameters.

Weibull

$$f(x;\mu,\kappa,\varepsilon)=\frac{\left(\frac{x-\varepsilon}{\mu-\varepsilon}\right)^{\varepsilon-1}}{\mu-\varepsilon}\kappa\, e^{-\left(\frac{x-\varepsilon}{\mu-\varepsilon}\right)^{\kappa}} \tag{A5}$$

where μ, κ and ε are adjustable parameters.

Chi χ

$$f(x;\alpha,\beta,\varepsilon)=\frac{2^{1-\frac{\alpha}{2}}}{\beta\Gamma\left(\frac{\alpha}{2}\right)}\left(\frac{x-\varepsilon}{\beta}\right)^{\alpha-1}e^{-\frac{1}{2}\left(\frac{x-\varepsilon}{\beta}\right)^2} \tag{A6}$$

where α, β, and ε are adjustable parameters.

Chi-Square χ^2

$$f(x;\alpha,\varepsilon)=\left(\frac{x-\varepsilon}{2}\right)^{\frac{\alpha}{2}-1}\frac{e^{-\left(\frac{x-\varepsilon}{2}\right)}}{2\Gamma\left(\frac{\alpha}{2}\right)} \tag{A7}$$

where α and ε are adjustable parameters.